Phase-field calculations of sink strength in Al, Ni, and Fe: A detailed study of elastic effects

Gabriel-Franck Bouobda Moladje, Ludovic Thuinet, Christophe Domain, Charlotte Becquart, A. Legris

Phase-field calculations of sink strength in Al, Ni, and Fe: a detailed study of elastic effects

Gabriel Franck Bouobda Moladje[a], Ludovic Thuinet[a,b,*], Christophe Domain[c,b], Charlotte S. Becquart[a,b], Alexandre Legris[a,b]

[a] *Univ. Lille, CNRS, INRAE, Centrale Lille, UMR 8207 - UMET - Unité Matériaux et Transformations, F-59000 Lille, France*
[b] *Laboratoire commun EDF-CNRS Etude et Modélisation des Microstructures pour le Vieillissement des Matériaux (EM2VM), France*
[c] *EDF-R&D, Département Matériaux et Mécanique des Composants (MMC), Les Renardières, F-77818 Moret sur Loing Cedex, France*

Abstract

The sink strength and bias of edge dislocations, low-angle symmetric tilt grain boundaries (STGBs), and spherical cavities are calculated for Al, Ni and Fe using a phase-field approach in this work. The interactions between point defects (PDs) and sinks are incorporated in the present model. These interactions include an elastic contribution to the total free energy of the system, and the phenomenon of elastodiffusion which is often ignored and consists in the modification of the PD migration energy due the strain field generated by the sink. Specific spatial schemes and new algorithms have been developed and applied to perform the calculations due to the PD diffusion which becomes anisotropic and spatial dependent when elastodiffusion is taken into account. The results obtained show that the solution of Rauh and Simon systematically underestimates the sink strength of edge dislocations, especially for dumbells in Ni and Fe. STGBs with low misorientation angle and high density are biased sinks when elasticity (with and without elastodiffusion) is taken into account. It is also shown that taking into account the PD anisotropy at saddle point when

*Corresponding author
Email address: ludovic.thuinet@univ-lille.fr (Ludovic Thuinet)

the elastodiffusion is considered leads to a significant bias ($> 10\%$) of the cavity, which thus highlights the importance of the PD anisotropy at saddle point on the sink strength and bias calculations.

Keywords: Phase-field, Irradiation, Sink strength, Elasticity, Elastodiffusion

1. Introduction

Predicting the microstructure evolution of structural materials of nuclear reactors during irradiation is a crucial issue for the nuclear industry. Under irradiation, point defects (PDs), self-interstitial atoms (SIAs) and vacancies, as well as point defect clusters are created and diffuse towards microstructural sinks such as dislocations, grain boundaries (GBs) and cavities. These microstructural defects evolve according to their ability known as sink strength to absorb PDs. Another interesting quantity called sink bias is commonly defined, which is the relative difference between the sink strengths for SIAs and vacancies. It allows explaining irradiation dislocation loop growth/shrinkage[1–3], irradiation void swelling [4], or irradiation creep [5–7].

Different methods are used to calculate the sink strength: analytical resolution of the PD diffusion equation around the considered sink [8, 9], object kinetic Monte Carlo simulations (OKMC) [10–13], or phase field (PF) approach [14–17]. The main advantage of the modelling techniques compared to the analytical models is the possibility to treat more complex microstructures and to incorporate the elastic interactions between PDs and sinks which may be addressed analytically only under simplifying conditions. This last point is important, since recent studies [12, 14] showed that elasticity has strong effects on the dislocation sink strength computation.

The elastic interactions between PDs and sinks induce supplementary energy contribution which acts as a driving force for PD diffusion. Moreover, the migration energies of PDs are also modified by the strain field generated by the

sink. This dependence is called elastodiffusion. It can be demonstrated that these two distinct effects are not redundant and appear when the continuum theory of diffusion is derived from the lattice theory of diffusion. This derivation has been an intense area of research and has been presented in the seminal work of [18] but also in [19, 20]. In this formalism, PDs are characterized by their elastic dipole tensors [13]. Several studies [12, 21, 22] addressed elastodiffusion effects on the sink strength calculations and on the role of the PD dipole tensor anisotropy at saddle point during PD diffusion. The analytical approach of elastodiffusion proposed in [21] showed the increase of the edge dislocation sink strength with the PD anisotropy at saddle point in fcc copper and bcc iron. Furthermore, they found that the anisotropy effects of the PD dipole tensor at saddle point were more pronounced for vacancies than SIAs in copper. More recently, the elastodiffusion effects on the edge dislocation sink strength were investigated in aluminium using OKMC simulations [12] and the results were qualitatively the same as those obtained in copper [21]. The results from [12] also showed that the bias associated to cavities can reach values greater than 10% by considering elastodiffusion, which means that a cavity cannot be considered as an unbiased sink as usually done [4]. GBs are usually considered as neutral sinks like cavities [4], but the investigation of the symmetric tilt grain boundary (STGB) stress field effects on its sink strength [23] revealed that STGBs with low misorientation angle may have significantly higher sink strengths due to elasticity effects, especially when their density is high. These results explain the interest of the elaboration of nanocrystalline materials for nuclear reactor designing. Indeed, experimental studies [24, 25] showed that nanocrystalline materials with high GB density can exhibit enhanced radiation resistance. In [22] it was also shown that elastic interactions between PDs and semicoherent interfaces lead to a marked enhancement of interface sink strength, especially

when elastodiffusion effects are taken into account.

This literature survey points out very interesting results concerning sink strengths of dislocations, STGBs or cavities but they are either limited to one particular material, which restricts the impact of their conclusions, or take only partially into account the elasticity effects, elastodiffusion being ignored in most of the cases. As a consequence, we propose in this paper a more systematic study of the sink strengths for these microstrutural defects for a panel of 3 materials, fcc Al, Ni and bcc Fe with a detailed description of elasticity effects, including elastodiffusion. This choice is driven by the fact that fcc Ni and bcc Fe are basic elements for nuclear materials and they belong at the same time to 2 different crystallographic structures. Concerning Al, it has already been studied in the literature and will be used thus as a case for comparison with the other studies. This choice should also allow to determine if the fcc materials exhibit the same tendencies or if significant differences are obtained between the fcc and bcc crystals of the present study.

The simulation technique used is based on a phase field approach since it allows to incorporate diffusion and elastic effects in its formalism and is well suited to treat a high diversity of microstructural defects, such as the ones mentioned above. In particular, a phase-field model was previously used to calculate dislocation and dislocation loop sink strengths in anisotropic materials such as Zr [14–16]. However, elastodiffusion was not considered in its formalism. This paper then proposes a new algorithm taking elastodiffusion into account in the phase field formalism. This is, to the authors' knowledge, the first attempt of this kind in the literature.

This paper is organized as follows. Section 2 presents the phase field methodology employed to calculate the sink strength, with a particular emphasis on the treatment of the different microstructural defects considered, as well as elastod-

iffusion. In section 3, the sink strength is computed in pure fcc Al, Ni and bcc metals for different sink types: edge dislocations, low-angle STGBs and spherical cavities. The results are discussed in section 4.

2. Phase field methodology

We consider a single cubic crystal in which one type of sink is introduced. PDs are created by irradiation at a uniform and constant generation rate K_0. Single PDs diffuse inside the matrix and are absorbed locally by the sink. To describe the system evolution under irradiation, the order parameters, the total free energy of the system and the evolution equations are defined successively, as usually done in a PF approach.

The necessary order parameters to describe the system evolution are the following:

i. The site fractions of PDs $X_d(\boldsymbol{r})$, $d = \text{I}$ for SIAs or V for vacancies.

ii. The elastic shape function $\eta_s(\boldsymbol{r})$ associated to the sink s, which is used to generate the corresponding stress field, if a correct eigenstrain $\varepsilon_{ij}^{0,\eta_s}$ is associated to this field. Its expression depends on the type of the microstructural defect and will be established later in this section.

iii. The shape function $\lambda_s(\boldsymbol{r})$ of the capture zone of sink s (equal to 0 inside the matrix and 1 in the capture zone). This parameter allows a precise control of the absorption of PDs by the sink, which is essential to correctly calculate the sink strength.

The PF model used in this paper has the particularity of using 2 distinct order parameters related to the microstructural defects instead of one as usually done: one simulates its stress field, the other one simulates its capture zone. This

method has already been tested in [14] and turns out to be efficient for the sink strength calculations.

The system evolves by minimisation of the total free energy F. Strictly speaking, this is only true close enough to equilibrium, an hypothesis that we assume in the following. F includes the chemical free energy F_{ch} associated to PD and the elastic energy F_{el}:

$$F(X_d, \eta_s) = F_{\mathrm{ch}}(X_d) + F_{\mathrm{el}}(X_d, \eta_s) \tag{1}$$

F_{ch} and F_{el} are respectively the chemical free energy associated to the PD and the elastic energy. In our system description, the sink evolution due to the PD absorption is not taken into account, and the sink is considered unchanged and immobile. This assumption is reasonable assuming a PD mobility higher than that of the sink, as is generally the case. In the following the self-free energy associated to the sink is ignored in Eq. 1. The chemical free energy in the limit of dilute solution is given by [4]:

$$F_{\mathrm{ch}}(X_d) = \frac{1}{\mathrm{V_{at}}} \sum_d \int_V E_f^d X_d + \mathrm{k_B} T [X_d \ln X_d + (1 - X_d) \ln(1 - X_d)] \quad dV \tag{2}$$

E_f^d is the PD formation energy, V_{at} the atomic volume, V the volume of the computational domain, $\mathrm{k_B}$ the Boltzmann constant, and T the temperature of the system. The elastic energy is calculated via the microelasticity theory [26] and is a function of the elastic strain which is the difference between the total strain $\varepsilon_{ij}(\boldsymbol{r})$ and the total eigenstrain $\varepsilon_{ij}^{0,\mathrm{tot}}(\boldsymbol{r})$ defined thereafter:

$$F_{\mathrm{el}} = \frac{1}{2} \int_V C_{ijkl} [\varepsilon_{ij}(\boldsymbol{r}) - \varepsilon_{ij}^{0,\mathrm{tot}}(\boldsymbol{r})][\varepsilon_{kl}(\mathbf{r}) - \varepsilon_{kl}^{0,\mathrm{tot}}(\boldsymbol{r})] \quad dV \tag{3}$$

where C_{ijkl} are the elastic constants of the system. In this work, the system is

considered as elastically homogeneous which means that the elastic constants are uniform in space. The total eigenstrain is given by:

$$\varepsilon_{ij}^{0,\mathrm{tot}}(\boldsymbol{r}) = \sum_{d} \varepsilon_{ij}^{0,X_d} X_d(\boldsymbol{r}) + \varepsilon_{ij}^{0,\eta_s} \eta_s(\boldsymbol{r}) \tag{4}$$

with ε_{ij}^{0,X_d} and $\varepsilon_{ij}^{0,\eta_s}$ respectively the eigenstrain tensors associated to the PD d in its stable equilibrium configuration and to sink s. In the elasticity theory, a PD can be modelled through its elastic dipole tensor P_{ij} which is related to the PD eigenstrain or Vegard's tensor by:

$$P_{ij}^{\mathrm{e},d} = V_{\mathrm{at}} C_{ijkl} \varepsilon_{kl}^{0,X_d} \tag{5}$$

$P_{ij}^{\mathrm{e},d}$ is the PD elastic dipole tensor at its stable state. The PD relaxation volume Ω_d is related to the Vegard coefficients through the relation:

$$\Omega_d = V_{\mathrm{at}} \mathrm{Tr}(\varepsilon_{kl}^{0,X_d}), \quad \mathrm{Tr}(\varepsilon_{kl}^{0,X_d}) = \sum_{k,l(k=l)} \varepsilon_{kl}^{0,X_d} \tag{6}$$

Elastic equivalences between sinks and inclusions are used to determine the corresponding eigenstrain $\varepsilon_{ij}^{0,\eta_s}$ [27–29]. Edge dislocations, low-angle GBs described as an array of edge dislocations, and spherical cavities are the sink geometries considered in this article. Proper PF simulation of dislocations became possible by means of the equivalence established by Nabarro [27], which states that a dislocation loop behaves elastically like a platelet inclusion with thickness d and whose border corresponds to the dislocation line. The eigenstrain ϵ_{ij}^{0,η_s} associated to the platelet is then defined as follows:

$$\varepsilon_{ij}^{0,\eta_s} = \frac{b_i n_j + b_j n_i}{2d} \tag{7}$$

b_i and n_j are respectively the i^{th} component of the Burgers vector and the j^{th} component of the unit vector normal to the habit plane of the loop. The field η_s allows to describe the position of the platelet: it is equal to 0 inside the matrix, and 1 inside the platelet and varies from 0 to 1 at the platelet border. The platelet border which corresponds to the dislocation loop core is therefore modelled as a diffuse interface of width w, typically set at 4 PF cells. In this paper, we use the Read and Shockley model [30], in which a low angle symmetric tilt grain boundaries (STGB) with the misorientation angle θ is described as an array of edge dislocations, separated by a distance h given by :

$$h = \frac{b}{2\sin(\theta/2)} \simeq \frac{b}{\theta} \tag{8}$$

As a consequence, a pile up of platelets (in which $\eta_s = 1$) is introduced in the PF computational domain in order to simulate pairs of STGB or equivalently nanotwins. The same eigenstrain as in Eq. 7 can be used. Following [31] we used the inclusion model of Eshelby [32] to determine the eigenstrain $\varepsilon_{ij}^{0,\eta_s}$ of a spherical cavity, which is in the absence of any external pressure [31]:

$$\varepsilon_{ij}^{0,\eta_s} = \frac{2\gamma}{R_{\text{cav}}(C_{1111} + 2C_{1122})(S_{1111} + 2S_{1122} - 1)}\delta_{ij} \tag{9}$$

where γ and R_{cav} are respectively the superficial tension and the radius of the cavity. δ_{ij} is the Kronecker symbol and S_{ijkl} the Eshelby tensor [31, 32]. The cavity surface is modelled as a diffuse interface of width 4 PF cells.

The total strain $\varepsilon_{ij}(\boldsymbol{r})$ can be decomposed into two parts, the heterogeneous part of the strain $\delta\varepsilon_{ij}(\boldsymbol{r})$ and the average strain $\overline{\varepsilon}_{ij}$:

$$\varepsilon_{ij}(\boldsymbol{r}) = \overline{\varepsilon}_{ij} + \delta\varepsilon_{ij}(\boldsymbol{r}) \tag{10}$$

it can be demonstrated that in elastically homogeneous systems,

$$\overline{\varepsilon}_{ij} = \sum_d \varepsilon_{ij}^{0,X_d} \overline{X_d(\boldsymbol{r})} + \varepsilon_{ij}^{0,\eta_s} \overline{\eta_s(\boldsymbol{r})} \tag{11}$$

where $\overline{X_d(\boldsymbol{r})}$ and $\overline{\eta_s(\boldsymbol{r})}$ are respectively the volume average values of $X(\boldsymbol{r})$ and $\eta_s(\boldsymbol{r})$. The heterogeneous strain $\delta\varepsilon_{ij}(\boldsymbol{r})$ derives from the displacement field $u_i(\boldsymbol{r})$ which is obtained by solving the mechanical equilibrium equation in the Fourier space [26, 33–36]:

$$C_{ijkl} \frac{\partial^2 u_k(\boldsymbol{r})}{\partial r_j \partial r_l} = C_{ijkl} [\sum_d \varepsilon_{kl}^{0,X_d} \frac{\partial X_d}{\partial r_j}(\boldsymbol{r}) + \varepsilon_{kl}^{0,\eta_s} \frac{\partial \eta_s}{\partial r_j}(\boldsymbol{r})] \tag{12}$$

The local PD flux $J_i^d(\boldsymbol{r},t)$ which is a linear function of driving force μ^d is given by:

$$J_i^d(\boldsymbol{r},t) = -\sum_j \frac{M_{ij}^d(\boldsymbol{r},t)}{V_{\mathrm{at}}} \nabla_j(\mu^d(\boldsymbol{r},t)) \tag{13}$$

where μ^d is the local energetic potential per PD:

$$\mu^d = \mathrm{V_{at}} \frac{\delta F}{\delta X_d} = \mu_{\mathrm{chem}}^d + \mu_{\mathrm{el}}^d \tag{14}$$

with

$$\mu_{\mathrm{chem}}^d = \mathrm{V_{at}} \frac{\delta F_{\mathrm{chem}}}{\delta X_d} \tag{15}$$

which, in the low PD fraction approximation, is given by:

$$\mu_{\mathrm{chem}}^d = E_f^d + \mathrm{k_B} T \ln X_d \tag{16}$$

and

$$\mu_{\mathrm{el}}^d = V_{\mathrm{at}} \frac{\delta F_{\mathrm{el}}}{\delta X_d} \tag{17}$$

$M_{ij}^d(\boldsymbol{r},t)$ is the mobility tensor of PD d which, in the case of the free energy of

Eq. 2, can be written as:

$$M_{ij}^{d}(\boldsymbol{r},t) = \frac{X_d(\boldsymbol{r},t)}{\mathrm{k_B}T} D_{ij}^{d}(\boldsymbol{r}) \tag{18}$$

where $D_{ij}^{d}(\boldsymbol{r})$ is the PD diffusion tensor. The PD diffusion equation is assumed to be of the Cahn-Hilliard type [37]. The generation rate term K_0 and the absorption term $J_{s,d}^{\mathrm{abs}}(\boldsymbol{r},t)$ are added in this equation to simulate the PD creation by irradiation and their local absorption by the sink. The resulting equation is given by:

$$\frac{\partial X_d}{\partial t}(\boldsymbol{r},t) = \sum_i \nabla_i [\sum_j \frac{D_{ij}^{d}(\mathbf{r})}{V_{\mathrm{at}}\mathrm{k_B}T} X_d(\boldsymbol{r},t) \nabla_j \mu^d(\mathbf{r},t)] + K_0 - J_{s,d}^{\mathrm{abs}}(\boldsymbol{r},t) \tag{19}$$

The recombination between PDs is neglected and the PD diffusion equations are solved independently. $J_{s,d}^{\mathrm{abs}}$ is defined by using the shape function λ_s according to:

$$J_{s,d}^{\mathrm{abs}}(\boldsymbol{r},t) = \lambda_s(\boldsymbol{r}) \lambda_{\mathrm{eff}} (X_d(\boldsymbol{r},t) - X_d^s) \tag{20}$$

λ_{eff} is an efficiency factor taken equal to $1/\delta t$ to maintain the PD atomic fraction inside the sink at X_d^s, δt is the time step used to evolve the kinetic equations. X_d^s is fixed at a constant value, usually taken as the thermal equilibrium fraction of PD. The shape function $\lambda_s(\boldsymbol{r})$ in the expression of the absorption term $J_{s,d}^{\mathrm{abs}}$ of Eq. 20 ensures the PD absorption only inside the sink, η_s and λ_s are assumed not to evolve with time since the sink is supposed to remain unchanged during the simulation.

Due to the cubic symmetry of the crystals and the nature of the point defects studied in this paper, the PD diffusion tensor in the unstrained system $D_{ij}^{0,d}$ is isotropic:

$$D_{ij}^{0,d} = D^{0,d} \delta_{ij} \tag{21}$$

However, during the diffusion of PDs towards the sink, the migration rate of PD is modified by the strain field. This phenomenon is called elastodiffusion. In the presence of an extended elastic strain field $\varepsilon_{kl}(\boldsymbol{r})$ generated by the sinks, the stable and saddle state energies E^{e} and E^{sad} are modified at the first order as follows:

$$E^{\mathrm{e}} = E_0^{\mathrm{e}} - \sum_{kl} P_{kl}^{\mathrm{e}} \varepsilon_{kl}(\boldsymbol{r}^{\mathrm{e}}) \tag{22}$$

$$E^{\mathrm{sad}} = E_0^{\mathrm{sad}} - \sum_{kl} P_{kl}^{\mathrm{sad}}(^{\boldsymbol{h}}_{\xi\psi}) \varepsilon_{kl}(\boldsymbol{r}^{\mathrm{sad}}) \tag{23}$$

where E_0^{e} and E_0^{sad} are respectively the PD energy at stable and saddle configurations in the unstrained system. P_{kl}^{e} and $P_{kl}^{\mathrm{sad}}(^{\boldsymbol{h}}_{\xi\psi})$ are respectively the elastic dipole tensors of PD at stable and saddle point for the jump direction $\mathbf{h}$ and for the initial ξ and final ψ PD orientations. Assuming that $\varepsilon_{kl}(\boldsymbol{r}^{\mathrm{sad}}) \simeq \varepsilon_{kl}(\boldsymbol{r}^{\mathrm{e}})$, it can be demonstrated that through an averaging procedure on all the possible jumps of PD d, the PD diffusion tensor is given by [18, 19]:

$$D_{ij}^{d}(\boldsymbol{r}) = \frac{3D^{0,d}}{NZ} \sum_{\boldsymbol{h}} \sum_{\xi\psi} u_i^{\boldsymbol{h}} u_j^{\boldsymbol{h}} \exp[\frac{1}{\mathrm{k_B}T} \sum_{kl} (P_{kl}^{\mathrm{sad}}(^{\boldsymbol{h}}_{\xi\psi}) - \bar{P}_{kl}^{\mathrm{e}}) \varepsilon_{kl}(\boldsymbol{r}^{\mathrm{e}})] \tag{24}$$

with $u_i^{\boldsymbol{h}}$ the i^{th} component of the unit vector in the direction of the jump $\boldsymbol{h}$, Z is the number of pairs (ξ,ψ) and N the number of nearest neighbour sites, $\bar{P}_{kl}^{\mathrm{e}}$ is given by:

$$\bar{P}_{kl}^{\mathrm{e}} = \frac{1}{3} \mathrm{Tr}(P_{kl}^{\mathrm{e}}) \delta_{kl} \tag{25}$$

The P_{ij}-tensors are determined from DFT based ab initio calculations described in section 3.1.

The sink strength $k_{s,d}^2$ can be deduced from Eq. 19 when steady state is reached. It is a function of the absorption rate $\overline{J_{s,d}^{\mathrm{abs}}}$ and the average site fraction

$\overline{X}_d$ [4]:

$$k^2_{s,d} = \frac{\overline{J^{\text{abs}}_{s,d}}}{D^{0,d}(\overline{X}_d - X^s_d)} \tag{26}$$

with

$$\overline{J^{\text{abs}}_{s,d}} = \frac{1}{V}\int_V \text{J}^{\text{abs}}_{s,d}(\boldsymbol{r})dV, \quad \overline{X}_d = \frac{1}{V}\int_V \text{X}_d(\boldsymbol{r})dV \tag{27}$$

The sink bias B_s is defined as [38]:

$$B_s = 1 - \frac{k^2_{s,\text{V}}}{k^2_{s,\text{I}}} \tag{28}$$

To solve the PD evolution equations, the following dimensionless parameters are introduced:

$$\begin{cases} \boldsymbol{r}^* &= \boldsymbol{r}/a_0, \quad \nabla^*_i = a_0\nabla_i \\ D^{d,*}_{ij} &= D^d_{ij}/D^{0,d} \\ t^* &= t/t_0, \quad t_0 = a^2_0/D^{0,d} \\ K^*_0 &= t_0 K_0 \\ J^{\text{abs},*}_{s,d} &= t_0 J^{\text{abs}}_{s,d} \\ C^*_{ijkl} &= C_{ijkl}/(\frac{\text{k}_\text{B}T}{V_{\text{at}}}), \quad \mu^{d,*} = \mu^d/\text{k}_\text{B}T \end{cases} \tag{29}$$

where a_0 is the length of a unit PF cell. The dimensionless form of Eq. 19 is then:

$$\frac{\partial X_d}{\partial t^*}(\boldsymbol{r}^*, t^*) = \sum_i \nabla^*_i[\sum_j D^{d,*}_{ij}(\boldsymbol{r}^*)X_d\nabla^*_j\mu^{d,*}(\boldsymbol{r}^*, t^*)] + K^*_0 - J^{\text{abs},*}_{s,d}(\boldsymbol{r}^*, t^*) \tag{30}$$

Eq. 24 shows that the PD diffusion tensor in strained system becomes anisotropic and spatial dependent due to elastodiffusion whereas it is isotropic and uniform in the unstrained system. In presence of elastodiffusion, solving the PD diffusion equation is then much more complex and time consuming, and specific

spatial schemes and new algorithms have been derived to treat Eq. 30. They are described in the Appendix A.

3. Results in pure fcc Al, Ni and bcc Fe

3.1. Input data

The simulations were performed at temperature $T = 300$ K and with the dimensionless PD generation rate $K_0^* = 3 \times 10^{-8}$. For this temperature, the thermal equilibrium fractions of PDs are generally small and thus we fixed the PD fraction inside the sink X_d^s close at $\simeq 0$. The elastic parameters for the simulations are given in table 1. The PD elastic dipole tensors necessary for elastodiffusion calculations in Al are available in [12] and recalled in table 1. The elastic dipole tensors of PDs in Ni and Fe were computed by DFT simulations using VASP [42, 43]. For this purpose, a periodic simulation cell of volume V containing a perfect crystal with N atoms is considered and relaxed. One PD is then introduced, the supercell vectors being kept fixed during atomic relaxation. If the PD is a vacancy (respectively SIA), the resulting number of atoms in the simulation supercell is N-1 (respectively N+1). The P_{ij}-tensors are deduced from the residual stress σ_{ij} induced by the PD on the simulation supercell through the relation [12, 13, 22]:

$$P_{ij} = V(\sigma_{ij} - \sigma_{ij}^0) \tag{31}$$

where σ_{ij}^0 is the residual stress on the perfect (without defect) supercell after relaxation which can be different from zero due to convergence limitations of the ab initio calculations. The calculations were performed in a periodic simulation box with 256 and 250 atoms for Ni and Fe respectively ($4 \times 4 \times 4$ and $5 \times 5 \times 5$ unit cells). The projector augmented wave method (PAW) was used and the exchange-correlation functional was evaluated with the Perdew-Burke-Ernzerhof

	Al	Ni	Fe
Elastic constants C_{11}, C_{12}, C_{44} (GPa)	106.51, 60.38, 27.8 [12]	250.8, 150, 123.5 [39]	243, 145, 116 [40, 41]
Eshelby constants S_{11}, S_{12}, S_{44}	0.5212, 0.0833, 0.2393	0.4481, 0.0852, 0.2759	0.4515, 0.0852, 0.2742
Anisotropy ratio $A = 2C_{44}/(C_{11}\text{-}C_{12})$	1.21	2.45	2.37
Elastic dipole tensor			
Stable point P^e_{ij} (eV)			
Vacancy	$\begin{bmatrix} -3.238 & 0 & 0 \\ 0 & -3.238 & 0 \\ 0 & 0 & -3.238 \end{bmatrix}$ [12]	$\begin{bmatrix} -5.448 & 0 & 0 \\ 0 & -5.448 & 0 \\ 0 & 0 & -5.448 \end{bmatrix}$	$\begin{bmatrix} -3.6368 & 0 & 0 \\ 0 & -3.6368 & 0 \\ 0 & 0 & -3.6368 \end{bmatrix}$
Dumbbell [100] for Al and Ni, [110] for Fe	$\begin{bmatrix} 19.652 & 0 & 0 \\ 0 & 18.518 & 0 \\ 0 & 0 & 18.518 \end{bmatrix}$ [12]	$\begin{bmatrix} 25 & 0 & 0 \\ 0 & 24.792 & 0 \\ 0 & 0 & 24.792 \end{bmatrix}$	$\begin{bmatrix} 20.6162 & -5.6702 & 0 \\ -5.6702 & 20.6162 & 0 \\ 0 & 0 & 24.8208 \end{bmatrix}$
Saddle point P^{sad}_{ij} (eV)			
Vacancy $\mathbf{h}$ = [110] for Al, Ni and $\mathbf{h}$ = [111] for Fe	$\begin{bmatrix} -2.866 & -0.080 & 0 \\ -0.080 & -2.866 & 0 \\ 0 & 0 & 1.000 \end{bmatrix}$ [12]	$\begin{bmatrix} -5.255 & -0.213 & 0 \\ -0.213 & -5.255 & 0 \\ 0 & 0 & 2.554 \end{bmatrix}$	$\begin{bmatrix} -3.2379 & -1.6342 & -1.6342 \\ -1.6342 & -3.2379 & -1.6342 \\ -1.6342 & -1.6342 & -3.2379 \end{bmatrix}$
Dumbbell ξ = [100] to ψ = [010], $\mathbf{h}$ = [110] for Al and Ni; ξ = [110] to ψ = [011], $\mathbf{h}$ = [111] for Fe	$\begin{bmatrix} 19.498 & 1.133 & 0 \\ 1.133 & 19.498 & 0 \\ 0 & 0 & 19.034 \end{bmatrix}$ [12]	$\begin{bmatrix} 25.438 & 1.492 & 0 \\ 1.492 & 25.678 & 0 \\ 0 & 0 & 25.411 \end{bmatrix}$	$\begin{bmatrix} 22.5000 & 2.8725 & -0.6864 \\ 2.8725 & 21.0942 & 2.8725 \\ -0.6864 & 2.8725 & 22.5000 \end{bmatrix}$
Relaxation volume Ω for dumbbell; vacancy			
Stable point Ω^e	$2.35V_{at}$; $-0.4V_{at}$	$1.98V_{at}$; $-0.43V_{at}$	$1.86V_{at}$; $-0.3V_{at}$
Saddle point Ω^{sad}	$2.394V_{at}$; $-0.189V_{at}$	$2.03V_{at}$; $-0.2V_{at}$	$1.8609V_{at}$; $-0.267V_{at}$
Relative variation of the relaxation volume $(\Omega^{sad} - \Omega^e)/\Omega^e$ for dumbbell; vacancy	0.0236; -0.5128	0.026; -0.5132	0.0006; -0.1096

Table 1: Elastic parameters for the simulations. The elastic dipole tensors are given in the basis $\mathfrak{B}_0$([100],[010],[001]). $\mathbf{h}$ is the migration direction of PD, ξ and ψ are respectively the initial and final configuration of the dumbbell.

(PBE) formulation. The plane wave energy cutoff was set to 350 eV for Ni and 300 eV for Fe, and the k-point grid mesh used was $3\times3\times3$. The most stable SIA configuration in fcc structures is generally the <100>-dumbbell [44] and in bcc structures the <111>-dumbbell, but in bcc iron it is the <110>-dumbbell which is the most stable due to magnetism [45]. The dumbbell migration mechanism is more complex than that of vacancies and the most favorable one for the [100] dumbbell in Al and Ni (respectively the [110] dumbbell in Fe) is a mechanism of translation-rotation from the [100] (respectively [110]) to the [010] (respectively [011]) orientation. The elastic dipole tensors for all the possible PD migration directions are deduced from each other by space rotations. As shown in Fig. 1, the choice of the PF basis $\mathfrak{B}_{\rm PF}(\mathbf{e}_1, \mathbf{e}_2, \mathbf{e}_3)$ is dictated by the orientation of the dislocations dipoles, and then does not correspond to the crystallographic basis $\mathfrak{B}_0$([100],[010],[001]). Therefore all the tensors must be rewritten in the PF basis using proper space rotations in the simulations. Different cases were chosen to investigate the elastodiffusion effects:

i. Case 1: no elastodiffusion, $P_{ij}^{\rm sad} \equiv P_{ij}^{\rm e}$.

ii. Case 2: isotropic PD at saddle point, $P_{ij}^{\rm sad} \equiv \frac{1}{3}Tr(P_{ij}^{\rm sad})\delta_{ij}$.

iii. Case 3: full elastodiffusion, real $P_{ij}^{\rm sad}$-tensors.

Cases 2 and 3 allows assessing the importance of the PD anisotropy at the saddle point.

3.2. Edge dislocation

A dipole of edge dislocations is considered as illustrated in Fig. 1-a), with the glide systems $\{111\}\langle\bar{1}10\rangle$ in fcc and $\{110\}\langle\bar{1}11\rangle$ in bcc. Each dislocation is characterised by:

a) its unit line vector: $\boldsymbol{l} = \frac{1}{\sqrt{6}}[\bar{1}\bar{1}\bar{2}]$ (fcc), $\frac{1}{\sqrt{6}}[\bar{1}1\bar{2}]$ (bcc)

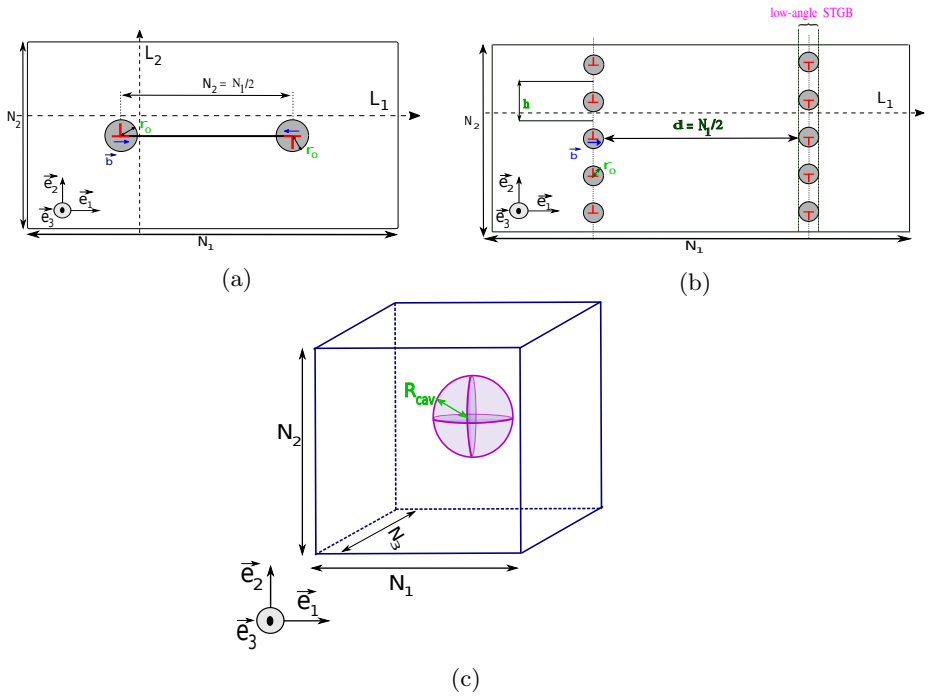

Figure 1: Simulation box containing a) a dipole of edge dislocations (2D), b) an array of edge dislocation dipoles (2D) or equivalently a low angle STGB, and c) a spherical cavity (3D).

b) its normal vector to the glide plane: $\boldsymbol{n} = \frac{1}{\sqrt{3}}[11\bar{1}]$ (fcc), $\frac{1}{\sqrt{2}}[110]$ (bcc)

c) its Burgers vector: $\boldsymbol{b} = \pm\frac{a}{2}[\bar{1}10]$ (fcc), $\pm\frac{a}{2}[\bar{1}11]$ (bcc), a is the lattice parameter.

The PF basis R_{PF} corresponds to $(\frac{1}{\sqrt{2}}[\bar{1}10], \frac{1}{\sqrt{3}}[11\bar{1}], \frac{1}{\sqrt{6}}[\bar{1}\bar{1}2])$ in Al and Ni, and to $(\frac{1}{\sqrt{3}}[\bar{1}11], \frac{1}{\sqrt{2}}[110], \frac{1}{\sqrt{6}}[\bar{1}1\bar{2}])$ in Fe. The size of a unit PF cell a_0 was taken equal to the length of the Burgers vector $\boldsymbol{b}$. The dislocation density ρ depends on the simulation box dimensions according to $\rho = \frac{2}{N_1 N_2 a_0^2}$ (see Fig. 1-a)). The capture region of the PD by the dislocation cores corresponds to 2 cylinders of radius r_0, where r_0 is set at 4b, a value which is close to the one proposed in the literature for pure bcc iron [46]. The shape function $\lambda_s(\mathbf{r})$ is equal to 0 outside the cylinder and 1 inside it.

The PD fluxes are plotted in Fig. 2 for each metal without (case 1) and with

full elastodiffusion (case 3). Overall, for both cases, dumbbells migrate preferen-

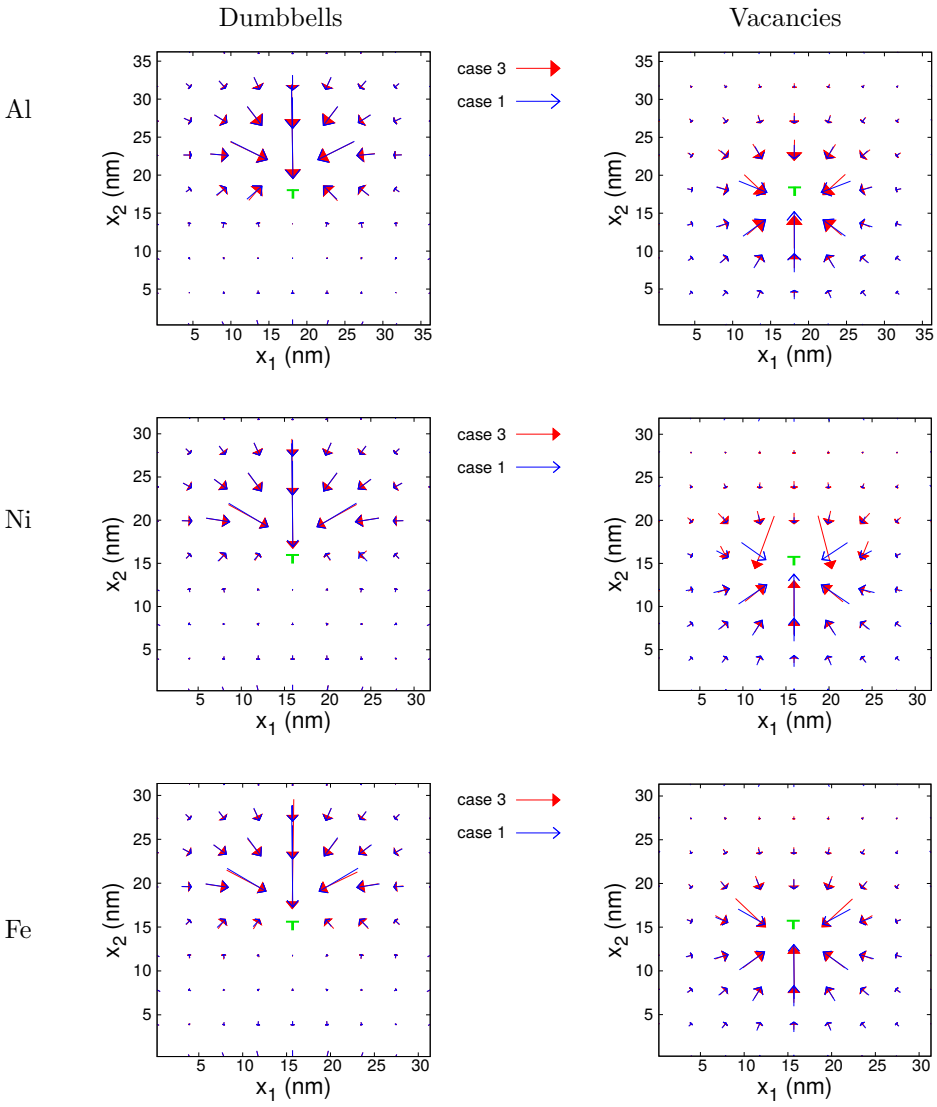

Figure 2: (Color online) Fluxes of dumbbells and vacancies in Al, Ni, and Fe, without elastodiffusion in blue (case 1) and with full elastodiffusion in red (case 3) for a dipole of edge dislocations. The length of the vector is proportional to the norm of the flux $\|\mathbf{J}\| = \sqrt{J_1^2 + J_2^2}$.

tially towards the tension region of dislocations. On the contrary, vacancies are more attracted to the compression region which is expected when elastic inter-

actions are considered. When the elastodiffusion is taken into account, the flow of dumbbells hardly changes for all the metals investigated here. Conversely, the trajectory of vacancies in all the metals is more affected by the elastodiffusion especially in the compression region. The flow intensity of vacancies decreases and its orientation changes near the compression region as shown in Figs. 2-b), 2-d) and 2-f).

In figure 3 are represented the sink strengths and the corresponding biases. The sink strength is higher with full elastodiffusion (case 3) compared to the case without elastodiffusion (case 1) in each metal and for each PD. This difference is amplified with the density of dislocations. The elastodiffusion effects are more significant for vacancies in all the metals.

We now examine intermediate case 2 to study the effects of PD anisotropy. In this case, the effect of elastodiffusion is due only to the change in the PD relaxation volume between stable and saddle points. The sink strength obtained in cases 1 and 2 are very close for dumbbells in all the metals. In the case of vacancies, elastodiffusion in case 2 induces a decrease of the sink strength in comparison to case 1 as shown in Fig. 3 in all the metals and this decrease is more marked in Ni. The relative difference of the relaxation volume $(\Omega^s - \Omega^e)/\Omega^e$ for dumbbells in all the metals and for vacancies in Fe is less or equal to 10% (see table 1). Thus the elastic interactions between PDs and dislocations at stable and saddle state configurations are practically the same in case 2 which explains the small change of the sink strength between cases 1 and 2. However, the relaxation volume of vacancies in Al and Ni at saddle state is significantly lower than the one at stable point. This leads to a strong decrease of the elastic interactions and thus to a decrease of the sink strength in case 2 in comparison to case 1.

The comparison between cases 1, 2 and 3 shows an increase of the sink

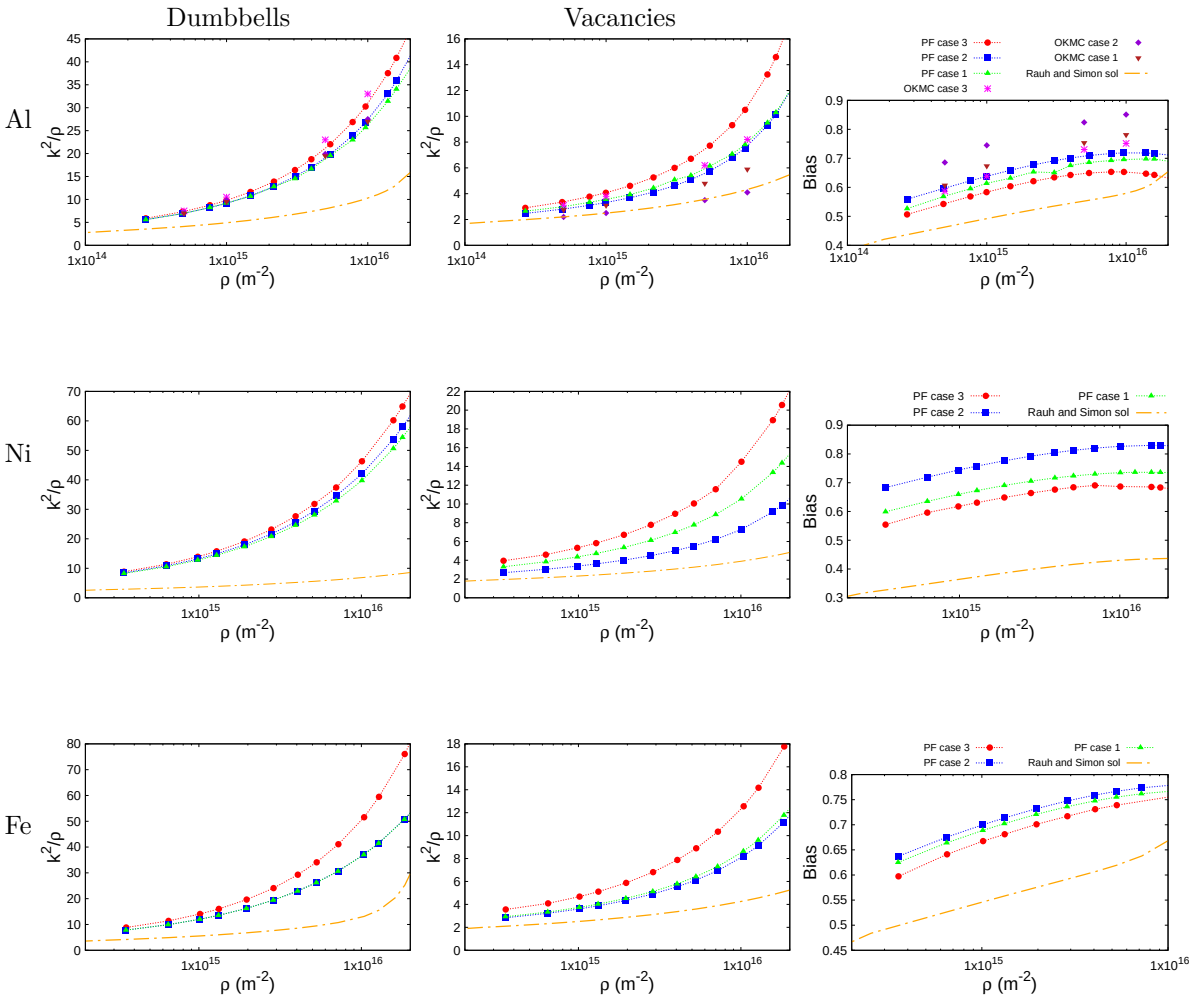

Figure 3: (Color online) Sink strength for dumbbells and vacancies, and bias as a function of the dislocation density in Al, Ni and Fe. Case 1: no elastodiffusion, case 2: elastodiffusion with isotropic PD at saddle point, case 3: full elastodiffusion.

strength with the PD anisotropy at saddle point. This increase is amplified with the dislocation density for vacancies in Al and Ni, and for both PDs in Fe. As a consequence the bias decreases when taking into account the PD anisotropy at saddle point in all the metals as illustrated in Fig. 3. The analytical solution of the sink strength proposed by Rauh and Simon [9] is also represented in figure

3. The results are comparable at low dislocation densities, but considerable differences are observed for high densities. The results obtained on all the 3 materials show that the analytical solution of Rauh and Simon (RS) strongly underestimates the values of the sink strength and consequently of the bias. For this latter quantity, the difference between the RS and PF results is particularly pronounced for Ni and Fe and can reach more than 20% in the case of Ni. This can be partly explained by the fact that the anisotropy ratio of Ni and Fe is large whereas the RS model is only valid for isotropic materials. These differences are due to several reasons already mentioned in [14]:

i. The Rauh and Simon solution is only valid for isotropic kinetic and elastic properties of systems and PDs. Moreover, elastodiffusion is ignored in this approach.

ii. To obtain the Rauh and Simon solution, the choice of the boundary conditions are similar to those of the Laplace's model [8, 14]. The PD atomic fraction used to compute the sink strength (see Eq. 26) corresponds to the atomic fraction at the boundaries of the reservoir instead of the mean value $\bar{X}$ as in the PF model.

iii. The Rauh and Simon model ignores the elastic interactions between the dislocations, which limits its validity to low dislocations densities.

The results obtained in [12] for sink strength and bias in Al using OKMC simulations are represented in figure 3. There is a good agreement between PF and OKMC results for low dislocation densities but differences are observed at high densities. This discrepancy can be explained by the fact that the radius r_0 of the PD capture region used in the OKMC simulations is equal to $2b$ while in the present study it is $4b$. In our PF model, $r_0 = w$ where w is the width of the dislocation core which is modelled as a diffuse interface. For numerical reasons

it is difficult to simulate an interface with less than 3 or 4 cells, hence the value chosen for r_0.

3.3. Low-angle symmetric tilt grain boundary (STGB)

The STGB is modeled by an array of edge dislocations as illustrated in Fig. 1-b). The array is characterized by 2 distances:

i. distance h between dislocations, related to the tilt angle θ: $h = b/\theta$.

ii. distance d between the 2 STGBs in the simulation domain.

Each dislocation has the same characteristics listed in section 3.2. The interspacing between dislocations h was set at $6b$ which corresponds to a misorientation angle of $\theta = 9.55°$. The radius r_0 of the capture zone is still equal to $4b$ for each dislocation like in section 3.2. The notation (hkl)[uvw] where (hkl) refers to the normal of the STGB plane and [uvw] to the tilt axis is adopted. Thus, the STGB in Al and Ni corresponds to the $(\bar{1}10)[\bar{1}\bar{1}\bar{2}]$ GB and in Fe to the $(\bar{1}11)[\bar{1}1\bar{2}]$ GB.

The PD fluxes towards the GB are plotted in Fig. 4. Like in the case of isolated straight edge dislocations ($\theta \to 0°$), dumbbells migrate preferentially in the tension region of each dislocation for all simulation cases and metals. On the contrary, vacancies migrate preferentially to the compression zone. The dumbbell trajectory changes very little in Al and Ni when full elastodiffusion is taken into account (case 3) compared to the case without (case 1). The same result is obtained for vacancies in Fe. However, in Ni the vacancy trajectory is strongly affected near the low angle STGB with full elastodiffusion. This is also the case for dumbbells in Fe.

The sink strength for PDs have been calculated and normalized by the sink strength of a neutral continuous planar sink without elastic interactions $k^2_{ps} = 12/(d-e)^2$ [23], e being the width of the planar sink which corresponds to the

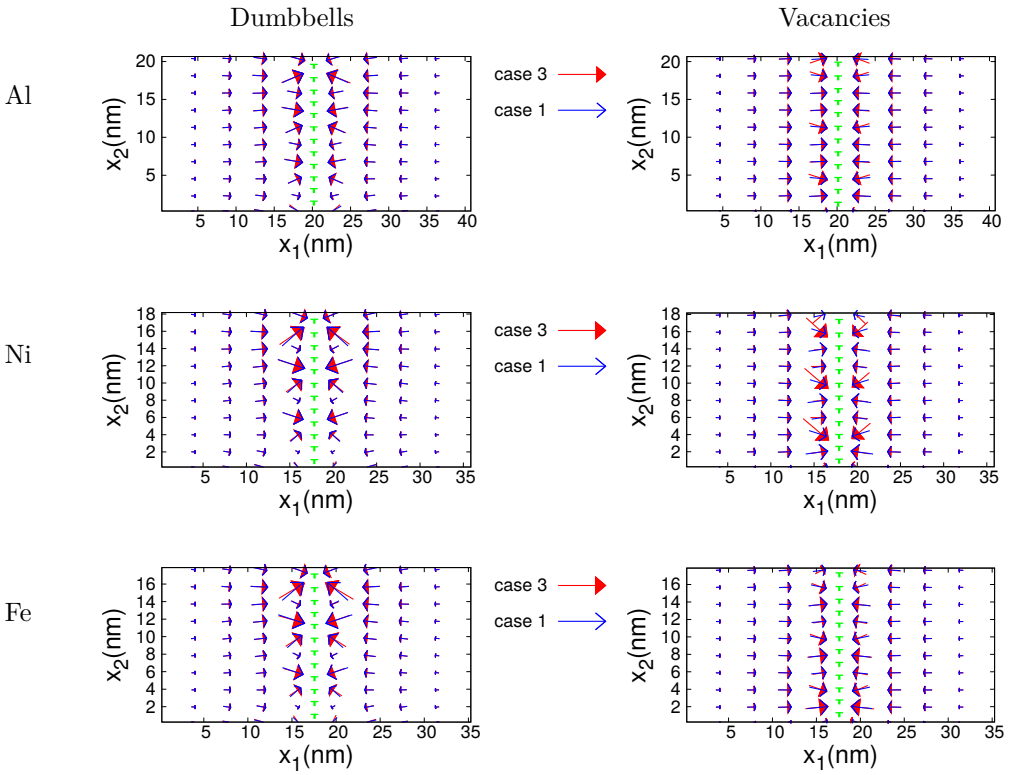

Figure 4: (Color online) Fluxes of dumbbells and vacancies in Al, Ni, and Fe, without elastodiffusion in blue (case 1) and with full elastodiffusion in red (case 3) for low angle STGB. The length of the vector is proportional to the norm of the flux $\|\mathbf{J}\| = \sqrt{J_1^2 + J_2^2}$.

width of the capture region $2r_0$ in our simulations. They are represented in Fig. 5 as well as the resulting sink bias. The sink strengths for both PDs, in all the simulation cases and in all the metals are very close to k_{ps}^2 for large STGB inter-spacing ($d > 30$ nm). The bias for these STGB inter-spacings is less than 10 %. For low STGB inter-spacings ($d < 30$ nm), the elastic effects become significant, which leads to a strongly biased STGB, especially for Fe in all the simulation cases. In particular for $d \simeq 5$ nm, the sink strength for vacancies is approximately twice times greater than k_{ps}^2 for all the cases, and the increase of the sink strength for dumbbells is even more significant. The

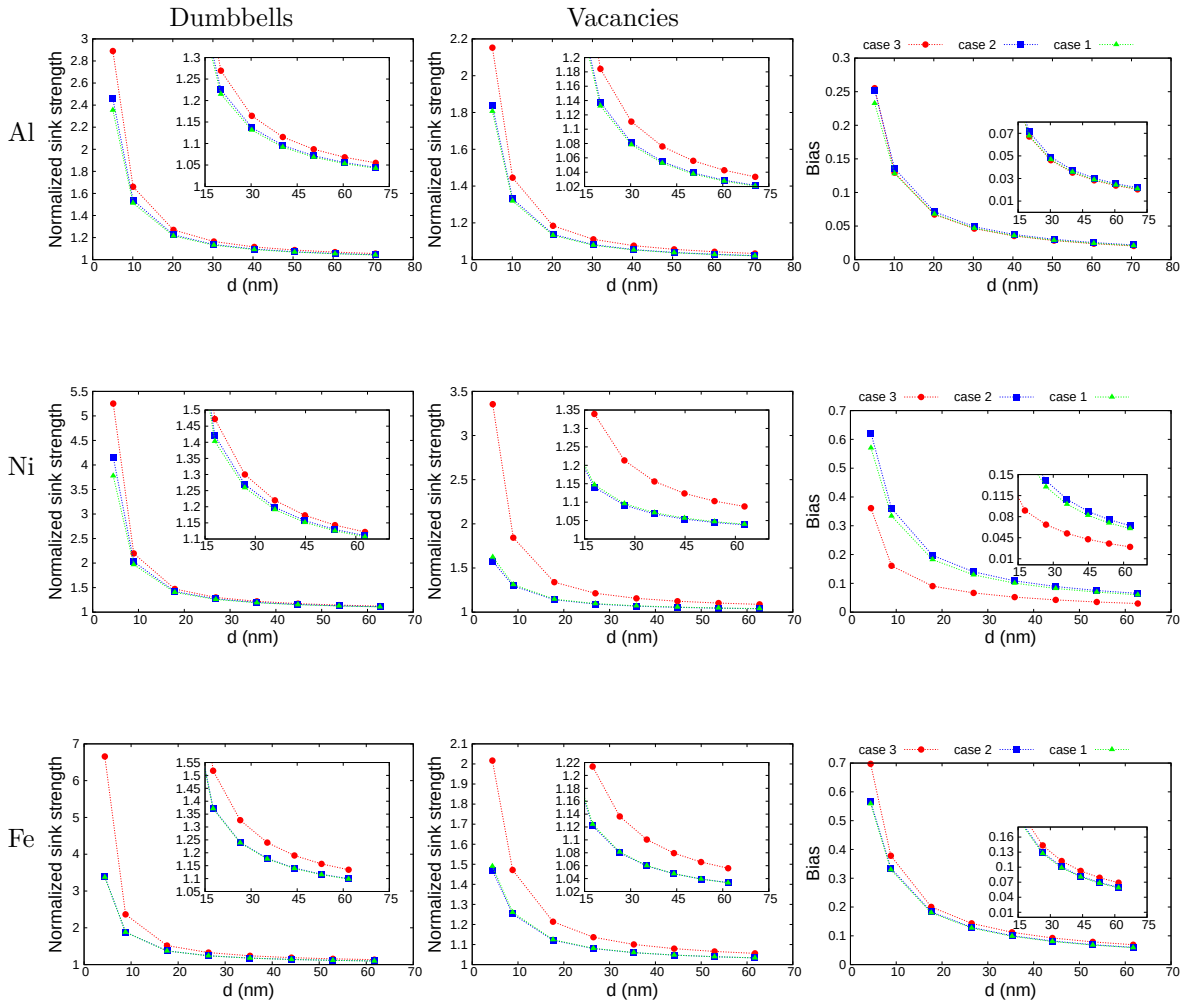

Figure 5: (Color online) Sink strength normalized by the sink strength of a neutral continuous planar sink for dumbbells and vacancies, and bias as a function of STGB inter-spacing in Al, Ni and Fe. Case 1: no elastodiffusion, case 2: elastodiffusion with isotropic PD at saddle point, case 3: full elastodiffusion.

sink strength is higher when full elastodiffusion (case 3) is taken into account compared to the cases 1 and 2, like in the case of isolated dislocations. In Al, the normalized sink strengths calculated in cases 1 to 3 are close for both PDs and the biases are then almost the same for all the simulations. In the case of Ni, full

elastodiffusion effects are more significant especially for vacancies and induce a strong decrease of the bias compared to the other cases. In Fe, elastodiffusion in case 2 has no effect on the sink strength for vacancies, but in case 3 an increase is observed for small STGB inter-spacings. For dumbbells, elastodiffusion does not change the sink strengths when dumbbells are considered isotropic at saddle point. However, with full elastodiffusion, the sink strength increases strongly for small STGB inter-spacings and leads to strong variations of the STGB bias as shown in Fig. 5 (bias $\simeq$ 70 % for $d \simeq 5$ nm).

The misorientation angle effect on the sink strength was also investigated by performing simulations with various values of the dislocation spacing h. Figure 6 shows the normalized sink strength and the sink bias for all the metals as a function of the misorientation angle θ, for a chosen GB inter-spacing. The results are qualitatively the same in all the metals. For both PDs, there is an increase followed by a decrease of the sink strength with θ, the maximum is obtained for a value of θ around $\simeq 3°$, the maximum being less visible for vacancies in Al and Fe. The representation of the bias given in Fig. 6-c) shows a decrease with the misorientation angle. These results concerning the influence of θ are very similar to those obtained in fcc Cu [23]. In this latter study, the maximum of the sink strength for dumbbells is around $\theta = 2°$. As explained in [23], the maximum observed on the curve representing the STGB sink strength as a function of θ is the result of 2 antagonistic effects:

i. The sink strength increases with the dislocation density ρ and consequently with θ as obtained in the case of isolated edge dislocations. Since in the case of STGB, $\rho = 1/hd = \theta/bd$, the sink strength should also increase with θ.

ii. However, for high dislocation densities (small h or high θ), the stress fields of neighboring STGB dislocations overlap strongly which leads to

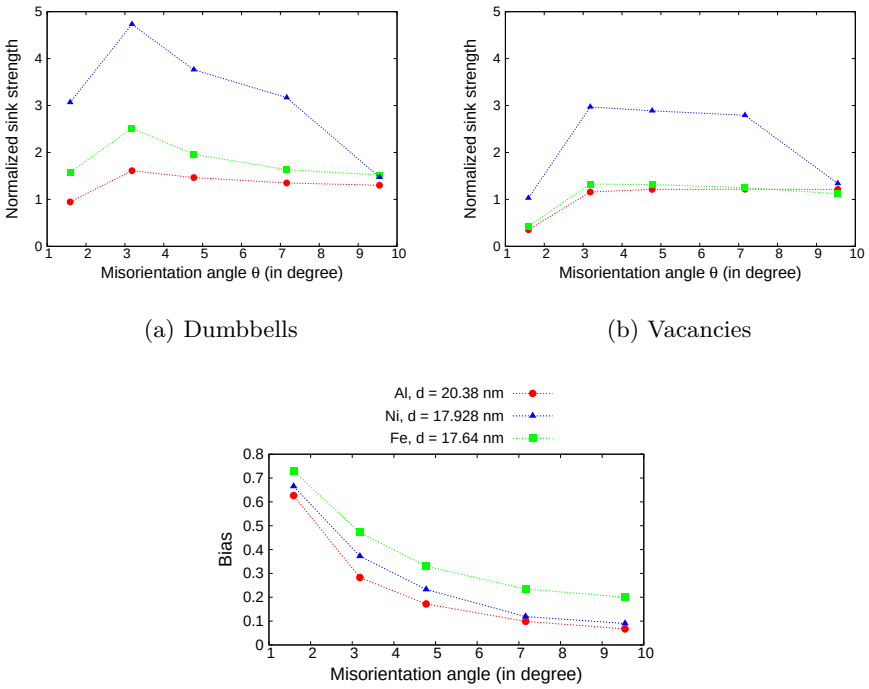

(a) Dumbbells

(b) Vacancies

(c) Bias

Figure 6: (Color online) Normalized sink strength for a) dumbbells, b) vacancies and c) sink bias as a function of the misorientation angle for a given STGB inter-spacing d in Al (red circle), Ni (blue triangle) and Fe (green square).

a mutual cancellation for the considered spatial arrangement. Thus, the STGB tends to act as a neutral continous planar sink without elastic stress field for high dislocation densities (high misorientation angles).

The maximum is less visible for vacancies due to their smaller relaxation volume than the one of dumbbells (see table 1) which implies weaker elastic interactions [23]. It can be concluded that the results of Figs. 5 for $\theta = 9.55°$ are in fact a low estimation of the bias: considering STGB with smaller misorientation angle of around 3° can lead to biases 2 to 3 times larger than the one obtained for 9.55°.

The crystal anisotropy effect was studied by changing the plane orientation

i.e. its normal **n** which is parallel to the Burgers vector **b**. The STGB orientation was changed from $(\bar{1}10)[\bar{1}\bar{1}\bar{2}]$ to $(100)[001]$ in Al, Ni and from $(\bar{1}10)[\bar{1}\bar{1}\bar{2}]$ to $(100)[001]$ in Fe. The results of the STGB bias calculations with full elastodiffusion are given in Fig. 7. In Al, the bias does not change much with

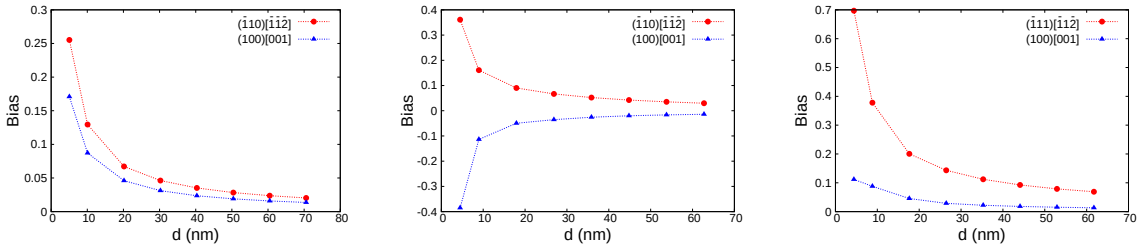

(a) (b) (c)

Figure 7: (Color online) Sink bias as a function of the STGB inter-spacing for different STGB orientations with full elastodiffusion in a) Al, b) Ni and c) Fe, $\theta = 9.55$ degree.

the STGB orientation. In Ni and Fe, the bias decreases from the $(\bar{1}10)[\bar{1}\bar{1}\bar{2}]$ to $(100)[001]$ and from the $(\bar{1}10)[\bar{1}\bar{1}\bar{2}]$ to $(100)[001]$ STGB respectively. This decrease is more pronounced for low STGB inter-spacings. In Ni, the bias of the $(100)[001]$ STGB even becomes negative for low STGB inter-spacings, which means that vacancies are more absorbed than dumbbells.

3.4. Spherical cavity

System description

A spherical cavity is located at the center of a 3D cubic PF simulation domain as illustrated in Fig. 1-c). The cavity radius was set at $R_{\text{cav}} = 1$ nm $(4a_0)$. The cavity surface was modelled as a diffuse interface with a width of 1 nm $(w = 4a_0)$. The radius of the capture region thus corresponds to $r_0 = 2$ nm $(r_0 = R_{\text{cav}} + w)$. The cavity density corresponds to $\rho = 1/N^3$ and the PF basis to $([100], [010], [001])$.

The PD flows towards the cavity are represented on Fig. 8 in the x_1x_2-plane

for a given cavity density. The trajectories of both PDs are almost normal

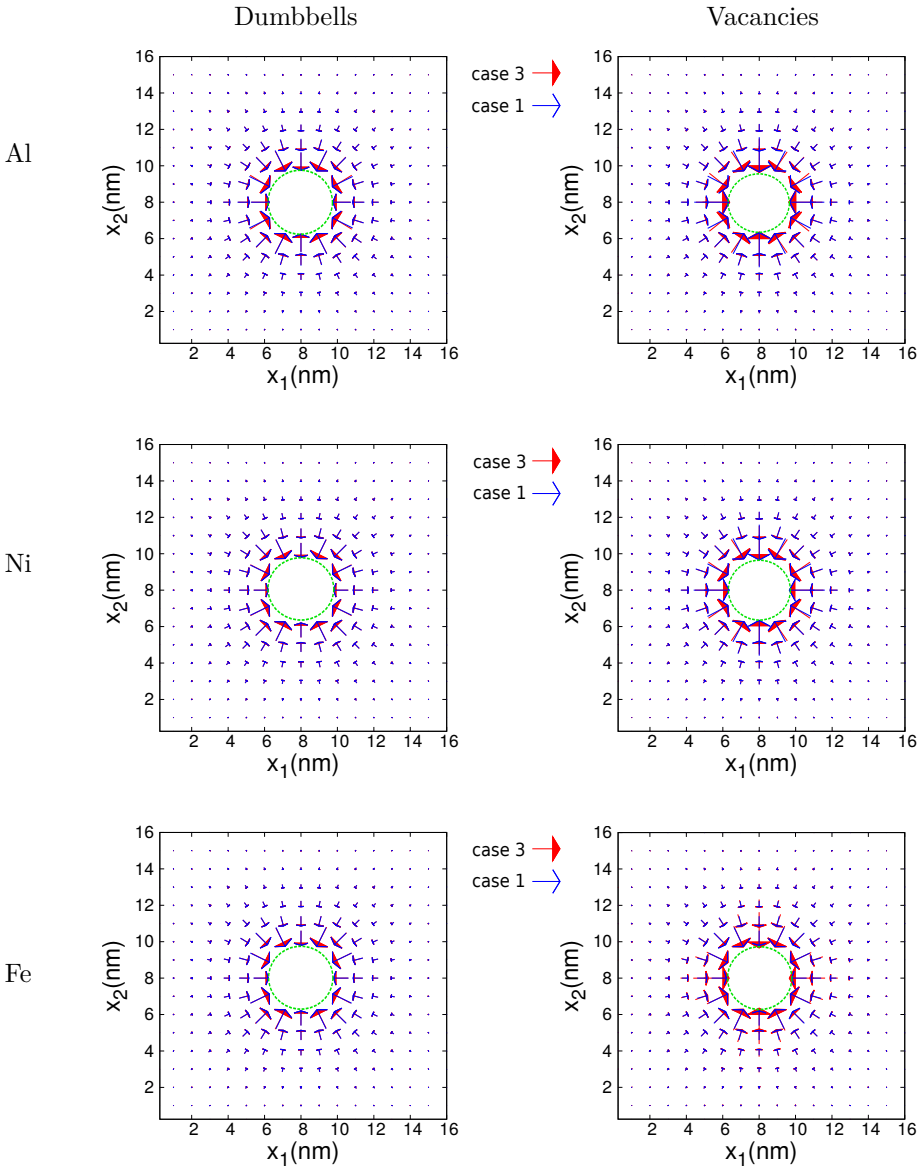

Figure 8: (Color online) Fluxes in the x_1x_2-plane of dumbbells and vacancies in Al, Ni, and Fe, without elastodiffusion in blue (case 1) and with full elastodiffusion in red (case 3) for a spherical cavity according to the x_1x_2-plane passing through the center of the cavity. The length of the vector is proportional to the norm of the flux $\|\mathbf{J}\| = \sqrt{J_1^2 + J_2^2}$.

to the surface of the cavity in all the simulation cases and for all the metals. The dumbbell trajectory does not change remarkably with the saddle point anisotropy in all the systems, as well as the trajectory of vacancies in Fe. On the other hand, a significant change is noted in the vacancy flow near the cavity in Al and Ni. As shown in Figs. 8-b) and 8-d) the vacancy trajectory is deflected in the vicinity of the cavity with the PD anisotropy at saddle point. The same effects of the P_{ij}-tensor anisotropy at saddle point on the PD trajectories near a spherical cavity in Al were obtained in [12].

The sink strengths and bias are plotted in Fig. 9. The sink strengths for PDs have been normalized by the sink strength of a neutral cavity without elastic interactions given by the Wiedersich formula:

$$k^2/\rho = \frac{4\pi r_0(1-f_d^{3/2})}{1-1.8f_d^{1/2}+f_d^{3/2}-0.2f_d^3} \tag{32}$$

where $f_d = (r_0/R)^2$ and $\rho = (\frac{4}{3}\pi R^3)^{-1}$, R being the reservoir radius. The sink strengths obtained for both PDs in cases 1 and 2 are close to the Wiedersich solution for all the systems. The bias in these cases is less than 5%. The results in the case of full elastodiffusion (case 3) show an increase of the sink strength for dumbbells and a decrease for vacancies compared to cases 1 and 2. As a consequence, the sink bias increases and is between 13% and 20% in Al, and around 10% in Ni and Fe for the corresponding cavity radius and cavity densities investigated ($10^{22} - 10^{24}\mathrm{m}^{-3}$). Thus, a cavity cannot be considered as a neutral sink when all the elastic effects are taken into account. It should also be noted that the bias varies slightly with the cavity density because a cavity produces a short-range strain field.

The bias evolution with the cavity radius R_{cav} was investigated and the results are represented in figure 10 along with the analytical solution of Borodin [29]. In Borodin solution, the radius of the capture region corresponds to the

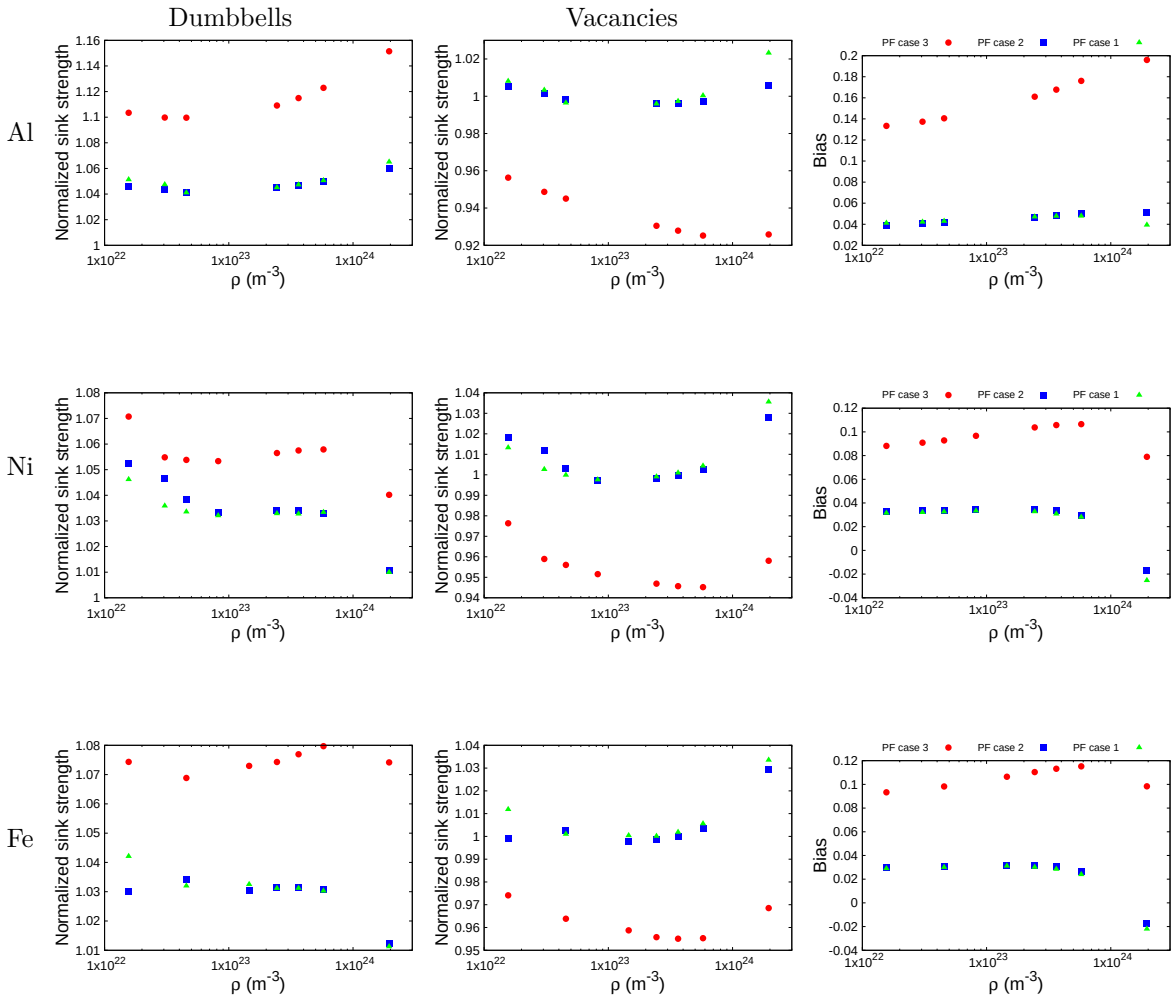

Figure 9: (Color online) Sink strength normalized by the Wiedersich solution as a function of the cavity density for dumbbells and vacancies, and bias in Al, Ni and Fe. Case 1: no elastodiffusion, Case 2: isptropic PD at stable and saddle points, Case 3: full elastodiffusion (real P_{ij}-tensors).

radius of the cavity ($r_0 = R_{\text{cav}}$). In our study, the capture radius of cavity is $r_0 = R_{\text{cav}} + w$ where w is the width of the cavity surface. The width of the cavity surface was then set at $4a_0$ ($a_0 = 0.25$ nm), and the capture radius to $r_0 = R_{\text{cav}} + 1$ nm. The bias is represented as a function of the sink capture

radius r_0 in Fig. 10. The results of Fig. 10 show a decrease of the cavity bias

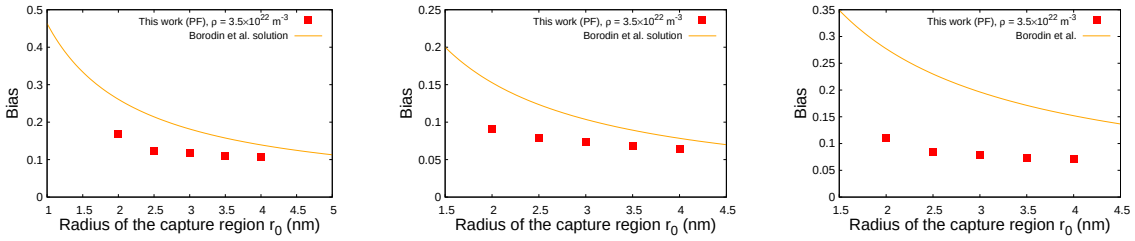

(a) (b) (c)

Figure 10: (Color online) Sink bias as a function of the cavity capture radius r_0 with full elastodiffusion in a) Al, b) Ni and c) Fe.

with its radius. This can be explained by the fact that the eigenstrain of the cavity is proportional to $1/R_{\text{cav}}$ (see Eq. 9) and the corresponding strain field decreases with R_{cav}. As a consequence the bias decreases with the cavity radius, since the elastic interactions decrease. In the cases of Al and Ni, we obtain a better agreement with the Borodin solution for large cavities than for small cavities. In Fe, there is a large difference between our results and the analytical solution of Borodin. Several reasons may explain these discrepancies:

i. The Borodin solution depends only on the elastic dipole tensor at saddle point and varies as $1/R_{\text{cav}}$.

ii. Dumbbells and vacancies are assumed to have the same P_{ij}-tensor symmetry at the saddle point in the Borodin solution. In our simulations, this is not the case for vacancies and dumbbells in Fe.

iii. The strain field around the cavity given in the Borodin solution corresponds to the one obtained considering an infinite isotropic medium.

iv. In our PF model, the cavity radius R_{cav} is different from the capture radius, which is not the case in the model of Borodin. However, when

increasing R_{cav}, this difference becomes relatively less significant. Besides, figure 10 shows that the results are closer for higher radii.

4. Discussion

In classical PF models, an interface energy for precipitate/cavity (or equivalently a core energy for the dislocation) is introduced in Eq. 1 and can be expressed as a function of the order parameter η_s. The expression of this term is then required to calculate the temporal evolution of η_s but not the ones of the other order parameters, in particular the diffusion equations of the PD site fractions X_d (the surface energy does not depend on X_d, and then gives no contribution to μ^d in Eq. 13 and 14). In our work, η_s does not evolve with time, in other words, the sink is supposed immobile and its expansion/regression is neglected during the simulation time (the idea is to make a correlation between the sink size and its strength), like in other approaches (Object Kinetic Monte Carlo [10–13, 22]) to calculate the sink strengths. As a consequence, since we do not calculate the temporal evolution of η_s, we do not need to express the interface energy in Eq. 1. This approach is the same as the one proposed in [14–17].

It has been shown that elastodiffusion modifies the flow of PD toward the sinks and the sink absorption bias. The magnitude of these effects depends strongly on the PD anisotropy at saddle point. In particular, the sink strength increases by taking into account the PD anisotropy at saddle point (case 3) compared to the other cases simulated (cases 1 and 2).

In all the metals and in the case of isolated edge dislocations, vacancies are more affected by elastodiffusion which induces a decrease of the sink bias around 5% or less, except in the case of Ni: taking into account full elastodiffusion or only isotropic elastodiffusion modifies the bias by more than 10%. The saddle

point anisotropy effects on the sink strength have been investigated by Skinner and Woo [21] in fcc Cu and bcc Fe at 500 K. Similar to what we find, they concluded that the sink strengh increases by a small amount for each PD and in each material. It should be noted that in the study of Skinner, <100>-dumbbells are considered as SIA in Cu and Fe while a <110>-dumbbell is considered in Fe for this study. The results obtained for Cu are very similar to those obtained in this study for Al and Ni. The normalized diffusion coefficients D_{ij}/D^0 are plotted in figure 11 to better investigate the elastodiffusion effects on PD diffusion. As shown by equation 24, the diffusion coefficients depend on the coupling between the P_{ij}-tensors at stable and saddle points and the strain field due to the sink. The profiles of Fig. 11 show stronger variations of the ratios D_{ij}/D^0 for vacancies than for dumbbells in Al and Ni, especially in Ni. These higher variations of the ratios D_{ij}/D^0 for vacancies allow to explain the decrease of the sink bias in Al and Ni with full elastodiffusion compared to the case without. In Fe, the magnitudes of the ratios D_{11}/D^0 and D_{12}/D^0 for both PDs are very close. Significant differences are observed for the ratio D_{22}/D^0, which is higher for dumbbells than for vacancies in some points (see Fig. 11), but overall a small decrease of the sink bias is observed with full elastodiffusion in Fe.

GBs are usually considered as neutral sinks in the literature [4]. The results obtained here show that for high STGB inter-spacings, the sink strengths for both PDs are weakly affected by the elastic stress field. As a consequence the STGB can be considered as neutral for high inter-spacings. However for low GB inter-spacings, this assumption is no longer valid and GBs act as biased sinks (see Fig. 5). The sink strength of STGBs can reach large values but for very low interspacings between them. However, these results are not so surprising if compared with some results of [22], in which a high enhancement of the sink

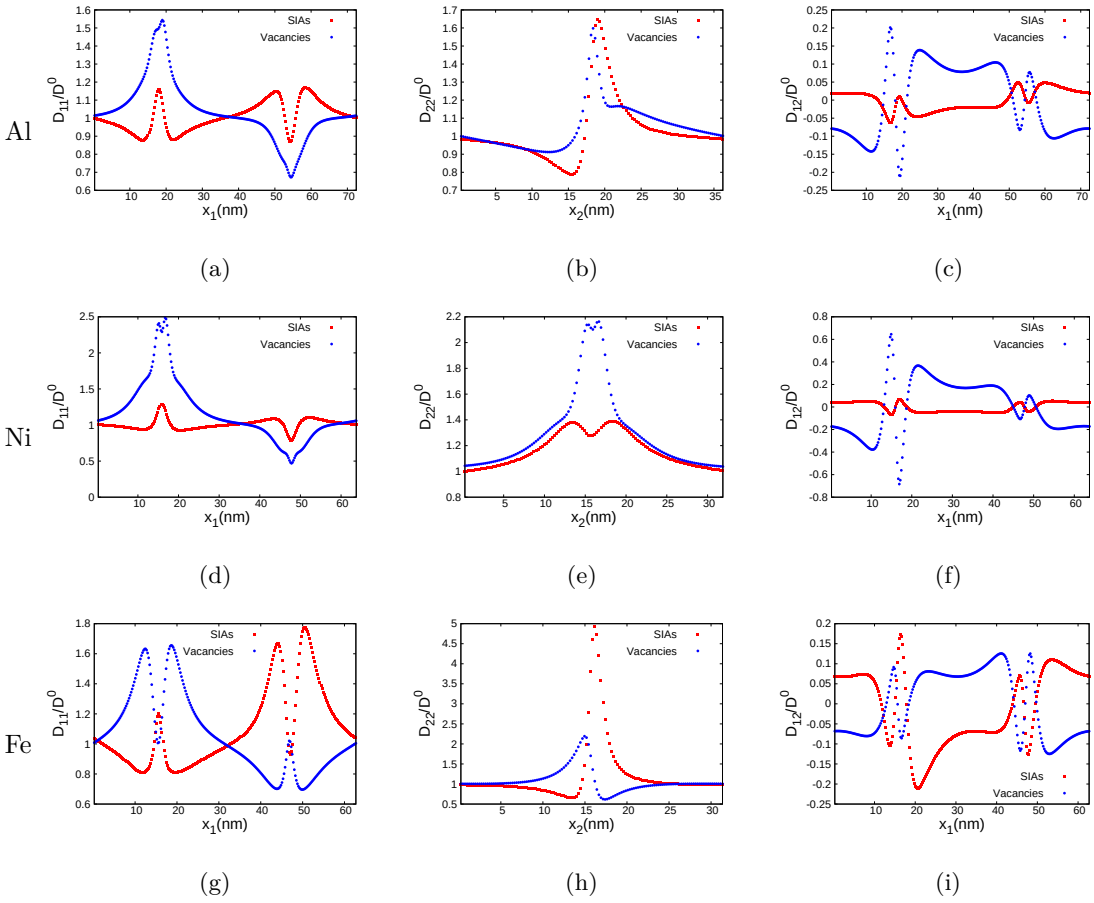

Figure 11: (Color online) Profiles of the normalized diffusion coefficients D_{11}/D^0 along $\mathbf{L}_1$ (see fig. 1-a)) at $x_2 = 21.22$ nm, D_{22}/D^0 along $\mathbf{L}_2$ (see fig. 1-a)) at $x_1 = 21.22$ nm and D_{12}/D^0 along $\mathbf{L}_1$ ($x_2 = 21.22$ nm) with full elastodiffusion (case 3) respectively a), b) and c) in Al, d), e) and f) in Ni, g), h) and ji) in Fe for a dipole of edge dislocations.

strengths is also observed for low interspacing values in Ag-Cu interfaces and Ag twist grain boundaries. For a value of d around 20 nm, the bias is approximately 7% for Al and 15% for Fe, whatever the simulation cases. STGB is thus significantly more biased in Fe than in Al. The case of Ni is more subtile since elastodiffusion effects are not negligible in this case. Without elastodiffusion, the bias is approximately the same as for Fe, whereas taking into account elastodiffusion divides its value by a factor 2, which illustrates the importance of

elastodiffusion in this particular case. The profiles of the normalized PD diffusion coefficients D_{ij}/D^0 obtained with full elastodiffusion are plotted in Fig. 12. As the STGB does not produce any long-range stress, the diffusion coefficients

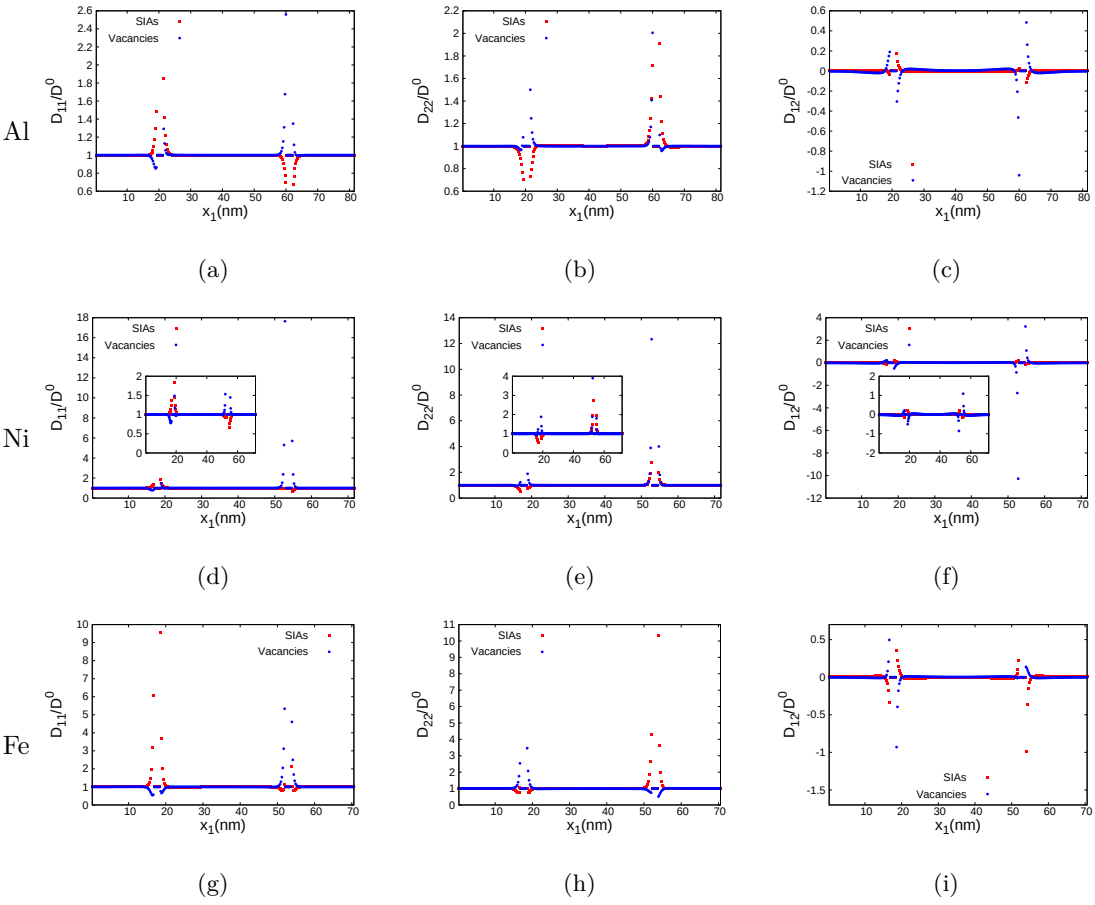

Figure 12: (Color online) Profiles of the normalized diffusion coefficients along $\mathbf{L}_1$ (see Fig. 1-b)) at $x_2 = 10.75$ nm, with full elastodiffusion (case 3) D_{11}/D^0, D_{22}/D^0 and D_{12}/D^0 respectively a), b) and c) in Al, d), e) and f) in Ni, g), h) and i) in Fe for a low angle STGB.

change only in the vicinity of the STGB. In Al and Ni, the variations of the ratio D_{ij}/D^0 are more important for vacancies than for dumbbells like in the case of isolated dislocations. These variations of the ratio D_{ij}/D^0 are small and remain comparable for both PDs in Al which explains the small change of the

sink strength and bias (see Fig. 5). In Ni, the variations are more pronounced for vacancies compared to dumbbells and this explains the strong effects of full elastodiffusion on sink strength for vacancies in this case. The ratio D_{ij}/D^0 in Fe varies strongly for both PDs. The variations are more pronounced for dumbbells which leads to the more noticeable effects of full elastodiffusion on sink strength for dumbbells in Fe. It must be pointed out that all these results were obtained for a fixed value of $\theta = 9.55°$, which has been arbitrarily chosen.

In [47], it is shown that the evolution of the bias with the grain boundary misorientation θ in Cu is not monotonous: for θ values between 3 and 10°, the bias increases with θ when the calculations include anisotropic elasticity and elastodiffusion, but this increase is very weak, the curve being almost a plateau in this range (the bias varies between 2 and 4%). Between 1 and 3°, the bias strongly increases when the misorientation decreases. This results in the presence of a shallow minimum in the curve $B(\theta)$ at θ around 3°. In figure 6 of our paper, we also plotted the curves $B(\theta)$ for each material under investigation Al, Fe and Ni but for none of them we obtained a minimum, instead B significantly decreases when θ increases for all the materials. Moreover, even in the θ-range $[3° - 10°]$, there is a more significant impact of elasticity than in [47] (for example, the bias varies between 5% and 30% for Al). This is mainly due to the distance between grain boundaries d, which is around 20 nm in our case whereas it is 70 nm in [47]. It means that the bulk volume fraction affected by the elastic field is larger in our case, which explains why the elasticity effects on the bias are more important in our study than in [47], even for larger values of θ. So it is possible that the minimum exhibited in figure 2 of [47] is erased in regimes where the elasticity effects are stronger. When comparing the data at the same value of d (around 60-70nm) and θ (around 10°), we observe that the bias is around 2% for Ni and Al and 6% for Fe (see figure 5 case 3: full elas-

todiffusion), which corresponds to the order of magnitude of the bias obtained in [47] (around 4%). This tends to confirm the importance of the parameter d in these calculations. The nature of the material may also play a role. In [47], the presence of a shallow minimum in the curve $B(\theta)$ is due to the fact that the maximum of the sink strength is not reached for the same misorientation for interstitials ($\theta = 1.5°$) and vacancies ($\theta = 3°$). In our case, the maximum of the sink strength for interstitials is always reached for the same value of θ (around 3°) whatever the material. For vacancies, the maximum of the sink strength is also reached at 3° for Ni but it is much less marked for Fe, and completely disappears for Al.

One limitation of our model is that the dislocations are supposed immobile. Gu et al [48] proposed an analytical approach to take into account the effect of climb on the sink strength of low-angle tilt grain boundaries, in the simplified case where only vacancies are considered and without taking into account the elastic interactions between PDs and dislocations. Their results clearly show that, for small misorientations, the GB sink strength drops rapidly to zero. The effect of the misorientation angle has also been investigated in our work, as shown in figure 6 and we observe the same tendency. However, the obtained curves are generally not monotonous in our case, but exhibit a maximum. This is due to the elastic interactions between PDs and dislocations, which are more significant when the misorientation angle is low, since the elastic fields of the dislocations in the STGB impinge on each other in a lesser extent. In [48], the specific contribution of climbing (in comparison to immobile dislocations) on the sink strength in not addressed.

In [49], a PF method is also developed to calculate the sink strength of low-angle symmetrical tilt grain boundaries. It is based on a different approach to describe the network of dislocations [50], and a PF dislocation climb model

[51–53], which allows to take into account the mobility of the dislocations due to climb. Dislocation climb is simulated by means of non-conserved dislocation dynamics to calculate the temporal evolution of the parameter η_s. In this work, the dimensionless parameter $L^* = Lb^2/M_0$ is introduced, with L a kinetic coefficient associated to the mobility of the dislocation, b the norm of the Burgers vector and M_0 the mobility of the vacancies. This parameter measures the difference between the speed of absorption of the vacancy in the core of the dislocation and the speed of arrival at the core. $L^* \gg 1$ means that the PDs are absorbed as soon as they arrive. When $L^* \gg 1$, their results are close to the ideal sink model based on an immobile array of dislocations (which corresponds to our work) for a misorientation angle θ of the grain greater than 4°. On the other hand, for lower values of θ there are significant deviations. This is due to the fact that during the climb there is a drag of vacancies, which is not the case in the static model. Thus the concentration of vacancies along the grain boundary is less important when the fast dislocation climb is included in the model and therefore the sink strength is greater. This phenomenon is closely related to the effective climb rate of the dislocations, which depends on several parameters. The first one is the quantity of PDs created in the bulk. In [49], it must be emphasized that the irradiation rate adopted in their simulations are quite high and it could be interesting to investigate if such an effect remains for lower values of K_0. The second one is the presence of self-interstitials, which are not considered in [49]. Then, the application of this model in its present form to dislocation evolution under irradiation is not straightforward and it still needs to be generalized in order to take into account both vacancies and interstitials. However, this type of models offers promising perspectives for a large panel of phenomena involving dislocations under irradiation and our work should in the future include climbing at least when the dislocation density is low in the grain

boundary.

The results of the sink strength and bias computations of a spherical cavity with elastodiffusion show that the PD anisotropy at saddle point leads to a significant change of the sink strength and bias in all the metals. Especially, the sink strength for SIAs increases, while the one for vacancies decreases when full elastodiffusion is considered. Therefore a cavity can no longer be considered as a neutral sink. This decrease of the cavity sink strength for vacancies is surprising, since in the case of an edge dislocation and a STGB we found an increase of the sink strength for both PDs when full elastodiffusion is taken into account. The diffusion coefficients hardly change with full elastodiffusion due to the small strain field generated by the cavity as illustrated on Fig. 13.

A condensed summary of all these results is given in table 2.

5. Conclusion

A PF model allowing to calculate the sink strength and bias of microstructural defects by taking into account the elastic interactions between sink and PDs is presented in this work. The added value of this model compared to the one presented in [14] is the incorporation of elastodiffusion effects, which allows a more precise sink strength calculation. A particular emphasis was placed on the role of the anisotropy of the PD elastic dipole tensors at saddle point on the sink trength and bias calculations. The simulations were performed for edge dislocations, STGBs and spherical cavities in pure fcc Al, Ni and bcc Fe metals.

The results show for all metals that the sink strengths of an edge dislocation and a low-angle STGB increase for both PDs with full elastodiffusion compared to the other cases of simulations, while the sink strength of a spherical cavity increases for dumbbells and decreases for vacancies with full elastodiffusion. The increase of the edge dislocation sink strength with full elastodiffusion is

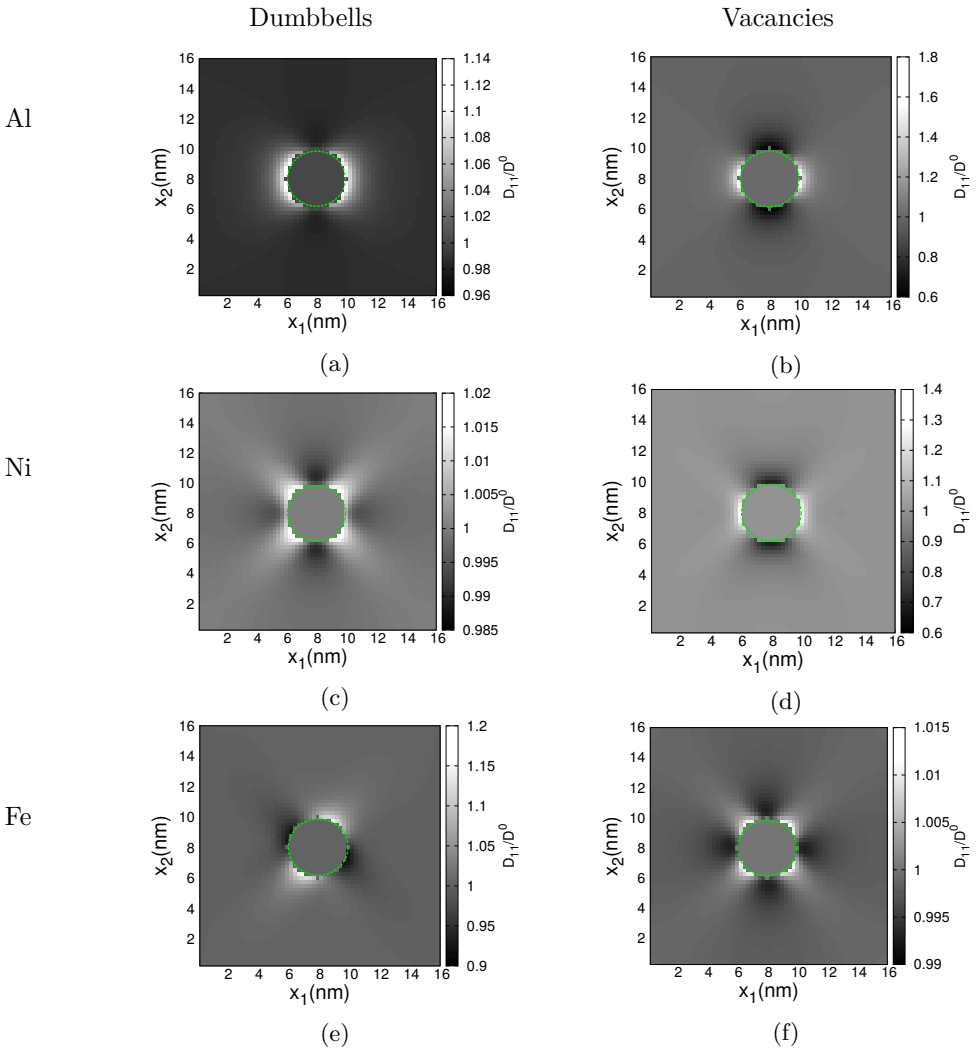

Figure 13: Maps of the normalized diffusion coefficient D_{11}/D^0 in the x_1x_2-plane passing through the center of the cavity with full elastodiffusion for dumbbells and vacancies respectively a) and b) in Al, c) and d) in Ni, e) and f) in Fe.

more important for vacancies than dumbbells in all the metals. This leads to the decrease of the dislocation sink bias. Furthermore, for all the simulation cases, the solution of Rauh and Simon systematically underestimates the sink strength, especially for dumbells in Ni and Fe. In the case of a low-angle STGB, the increase of the sink strength with full elastodiffusion is almost the same

STGBs with low misorientation angle and low inter-spacing are biased sinks in all the metals and all the cases of the simulation.

Spherical cavities are biased sinks in the case 3 of the simulation, in all the metals.

	Al	Ni case 3 compared to cases 1 and 2	Fe
		Sink strength for dumbbells	
Edge dislocation	Increased	Increased	Increased
Low-angle STGB	Increased	Increased	Increased
Spherical cavity	Increased	Increased	Increased
		Sink strength for vacancies	
Edge dislocation	Increased	Increased	Increased
Low-angle STGB	Increased	Increased	Increased
Spherical cavity	Decreased	Decreased	Decreased
		Sink bias	
Edge dislocation	Decreased	Decreased	Decreased
Low-angle STGB	Hardly changed	Decreased	Slightly increased
Spherical cavity	Increased	Increased	Increased

Case 1: without elastodiffusion.
Case 2: with elastodiffusion and isotropic elastic dipole tensor at saddle point.
Case 3: with elastodiffusion and real elastic dipole tensor at saddle point.

Table 2: Summary of the results.

for both PDs in Al and Fe which leads to a small change of the sink bias in this two metals. Contrariwise, vacancies are more affected by the increase of the sink strength with full elastodiffusion in Ni and this leads to the STGB sink bias decrease. The STGB sink bias in all the metals increases significantly with the decrease of the STGB inter-spacing on the one hand, and with the decrease of the misorientation angle on the other hand. An important issue to emphasize is that STGBs with high density and low misorientation angle have high sink strengths and are strongly biased. Moreover, the STGB sink bias changes significantly with the STGB orientation in Ni and Fe, while the change is not so remarkable in Al. As with full elastodiffusion the sink strength of the cavity decreases for vacancies in all the metals, the cavity bias increases and is

close to 10% for small radius which is not negligible. Thus cavities with small radii can no longer be considered as neutral sinks. There is a decrease of the cavity bias with the increase of the radius in all the metals, but this decrease is not marked. The comparison of the cavity sink bias with the solution of Borodin reveals important discrepancies in the case of Fe.

The results are qualitatively the same for all the metals as shown in table 2. These results can have direct consequences on dislocation loop and cavity growth or shrinkage rates. These quantities are essential in the understanding of several phenomena occurring during irradiation ageing such as irradiation creep or swelling. The prediction of the radiation induced segregation (RIS) a phenomenon that results from the coupling between PD and atom fluxes can be also affected by elastodiffusion and will be investigated in future works.

Declaration of Competing Interest

None.

Credit author statement

Gabriel F. Bouobda Moladje: Conceptualization, Methodology, Software, Validation, Formal Analysis, Investigation, Writing - Original draft. **Ludovic Thuinet**: Conceptualization, Methodology, Resources, Writing - Original draft, Supervision, Project Administration. **Christophe Domain**: Software, Data Curation, Writing - Original draft. **Charlotte S. Becquart**: Resources, Writing - Original draft, Supervision, Project Administration, Funding Acquisition. **Alexandre Legris**: Resources, Writing - Original draft, Supervision, Project Administration, Funding Acquisition.

Acknowledgements

– We are grateful to Antoine Ruffini for helpful discussions.

– This work was supported by the Euratom research and training programme 2015-2019 under Grant Agreement No 661913 (SOTERIA).

– The authors thank the Centre de Ressources Informatiques of the université de Lille (CRI) for computational facilities.

Data Availability

The raw/processed data required to reproduce these findings cannot be shared at this time as the data also forms part of an ongoing study.

Appendix A

An explicit Euler scheme is used to solve Eq. 30:

$$X_d^{t^*+\delta t^*} = X_d^{t^*} + (\frac{\partial \mathrm{X}_d}{\partial t^*})^{t^*} \delta t^* \tag{A-1}$$

A finite difference scheme is used for the spatial discretization involving the following dimensionless classical derivative operators:

$$\nabla_1^{*,c}\phi(r_1^*, r_2^*, r_3^*) = \frac{[\phi(r_1^*+1, r_2^*, r_3^*) - \phi(r_1^*-1, r_2^*, r_3^*)]}{2} \tag{A-2}$$

$$\tilde{\nabla}_1^{*,c}\tilde{\phi}(q_1^*, q_2^*, q_3^*) = \frac{[\exp(i_c q_1^*) - \exp(-i_c q_1^*)]}{2}\tilde{\phi}(q_1^*, q_2^*, q_3^*) \tag{A-3}$$

where $\tilde{\nabla}_1^{*,c}$ is the Fourier transform of the gradient operator $\nabla_1^{*,c}$, ϕ any field, $\mathbf{q}$ the wave vector and i_c the imaginary complex number defined as $(i_c)^2 = -1$. $\nabla_2^{*,c}$ and $\nabla_3^{*,c}$ (respectively $\tilde{\nabla}_2^{*,c}$ and $\tilde{\nabla}_3^{*,c}$) are defined in the same way as

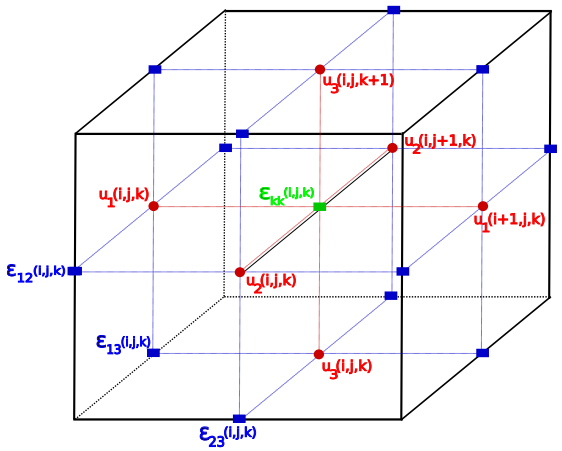

Figure A-1: Staggered finite difference grids [54]. The total volume represents a unit PF cell.

$\nabla_1^{*,c}$ (respectively $\tilde{\nabla}_1^{*,c}$). To overcome the appearance of artifact oscillations, the displacement and the strain fields are evaluated on staggered grids [54–56] schematized in Fig. A-1. Shifted derivative operators are introduced and defined as:

$$\nabla_1^{*,+}\phi(r_1^*, r_2^*, r_3^*) = \phi(r_1^* + 1, r_2^*, r_3^*) - \phi(r_1^*, r_2^*, r_3^*) \tag{A-4}$$

$$\nabla_1^{*,-}\phi(r_1^*, r_2^*, r_3^*) = \phi(r_1^*, r_2^*, r_3^*) - \phi(r_1^* - 1, r_2^*, r_3^*) \tag{A-5}$$

$$\tilde{\nabla}_1^{*,+}\tilde{\phi}(q_1^*, q_2^*, q_3^*) = (\exp(i_c q_1^*) - 1)\tilde{\phi}(q_1^*, q_2^*, q_3^*) \tag{A-6}$$

$$\tilde{\nabla}_1^{*,-}\tilde{\phi}(q_1^*, q_2^*, q_3^*) = (1 - \exp(-i_c q_1^*))\tilde{\phi}(q_1^*, q_2^*, q_3^*) \tag{A-7}$$

An important fact about using staggered grids is that one staggered grid is dedicated to the diagonal components of the strain tensor, and others to each off-diagonal component as shown on Fig. A-1.

To prevent also the appearance of artifact oscillations during the resolution of the PD evolution equation, a staggered grid is employed to compute the PD flux as done in [57]. This new scheme allows to handle numerical instabilities which can occur due to sharp variations of the diffusion tensor when elastodiffusion is taken into account. The PD flux is rewritten using the shifted derivative operators:

$$J_i^{d,*\pm}(\boldsymbol{r}^*,t^*) = -\sum_j D_{ij,j}^{d,*\pm}(\boldsymbol{r}^*) X_{d,j}^{\pm}(\boldsymbol{r}^*,t^*) \nabla_j^{*,\pm} \mu^{d,*}(\boldsymbol{r}^*,t^*) = \sum_j J_{i,j}^{d,*\pm}(\boldsymbol{r}^*,t^*) \tag{A-8}$$

with

$$J_{i,j}^{d,*\pm}(\boldsymbol{r}^*,t^*) = D_{ij,j}^{d,*\pm}(\boldsymbol{r}^*) X_{d,j}^{\pm}(\boldsymbol{r}^*,t^*) \nabla_j^{*,\pm} \mu^{d,*}(\boldsymbol{r}^*,t^*) \tag{A-9}$$

where

$$D_{ij,1}^{d,*-}(r_1^*,r_2^*,r_3^*) = \frac{D_{ij}^*(r_1^*,r_2^*,r_3^*) + D_{ij}^*(r_1^*-1,r_2^*,r_3^*)}{2} \tag{A-10}$$

$$D_{ij,1}^{d,*+}(r_1^*,r_2^*,r_3^*) = \frac{D_{ij}^{d,*}(r_1^*+1,r_2^*,r_3^*) + D_{ij}^*(r_1^*,r_2^*,r_3^*)}{2} \tag{A-11}$$

$$X_{d,1}^{-}(r_1^*,r_2^*,r_3^*,t^*) = \frac{X_d(r_1^*,r_2^*,r_3^*,t^*) + X_d(r_1^*-1,r_2^*,r_3^*,t^*)}{2} \tag{A-12}$$

$$X_{d,1}^{+}(r_1^*,r_2^*,r_3^*,t^*) = \frac{X_d(r_1^*+1,r_2^*,r_3^*,t^*) + X_d(r_1^*,r_2^*,r_3^*,t^*)}{2} \tag{A-13}$$

$J_i^{d,*+}$ and $J_i^{d,*-}$ are respectively the PD flux shifted to the right and to the left. In other words, the PD flux is evaluated at the middle of the PF cell boundaries as illustrated in Fig. A-2. The dimensionless diffusion equation 30 becomes:

$$\frac{\partial \mathrm{X}_d}{\partial t^*}(\boldsymbol{r}^*,t^*) = -\sum_i \sum_j \nabla_i^{*,\mp} J_{i,j}^{d,*\pm}(\boldsymbol{r}^*,t^*) + K_0^* - J_{s,d}^{abs,*}(\boldsymbol{r}^*,t^*) \tag{A-14}$$

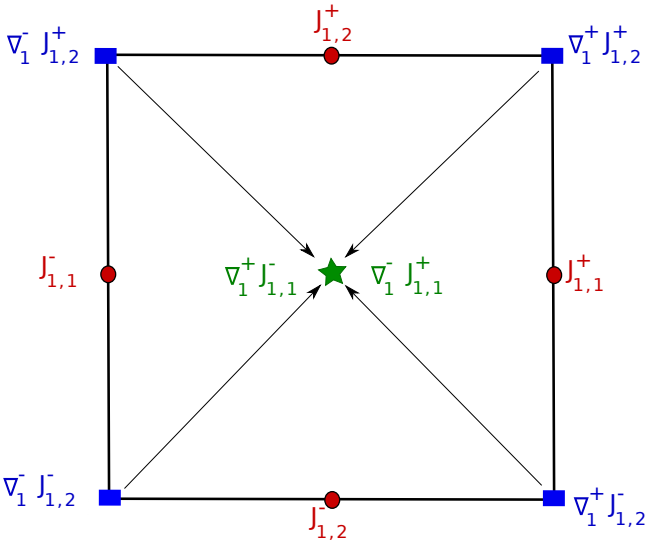

Figure A-2: 2D reprentation of the staggered grid used to compute the PD flux and its divergence. The superscripts $(*, d)$ have been omitted for clarity.

where

$$\nabla_i^{*,\mp} J_{i,j}^{d,*\pm} = \begin{cases} -\nabla_i^{*,-} J_{i,i}^{d,*+} & \text{or equivalently} \\ -\nabla_i^{*,+} J_{i,i}^{d,*-} & \text{if} \quad \text{i} = \text{j} \end{cases} \tag{A-15}$$

and

$$\nabla_i^{*,\mp} J_{i,j}^{d,*\pm} = -\frac{1}{4}[\nabla_i^{*,-} J_{i,j}^{d,*+} + \nabla_i^{*,-} J_{i,j}^{d,*-} + \nabla_i^{*,+} J_{i,j}^{d,*-} + \nabla_i^{*,+} J_{i,j}^{d,*+}]$$

$$\text{if} \quad \text{i} \neq \text{j} \tag{A-16}$$

This discretization scheme shows that for the diagonal terms of the PD diffusion tensor, the divergence of the PD flux given by $\nabla_i^{*,\mp} J_{i,j}^{d,*\pm}$ is evaluated at the center of the PF cells. On the other hand for off-diagonal terms, $\nabla_i^{*,\mp} J_i^{d,*\pm}$ is calculated at the corner of the PF cell boundaries as shown in Fig. A-2. To have the divergence of the PD flux at the center of the PF cells, an average value of all the terms $\nabla_i^{*,\mp} J_{i,j}^{d,*\pm}$ given at each corner is done. In practice, the

discretization scheme is more stable when it is only the chemical flux $J^{d,*}_{chem}$ which is evaluated on shifted grids. This may due to the fact that the elastic potential $\mu^{d,*}_{el}$ and the diffusion coefficients $D^{d,*}_{ij}$ which depend on the strain field are computed using the shifted derivative operators.

References

[1] L. L. Horton, J. Bentley, K. Farrell, A TEM study of neutron-irradiated iron, Journal of Nuclear Materials 108-109 (1982) 222–233. doi:10.2172/6659613.

[2] A. H. Duparc, C. Moingeon, N. S. de Grande, A. Barbu, Microstructure modelling of ferritic alloys under high flux 1 MeV electron irradiations, Journal of Nuclear Materials 302 (2002) 143–155. doi:10.1016/s0022-3115(02)00776-6.

[3] Y. Li, S. Hu, C. H. H. Jr, H. Deng, F. Gao, X. Sun, M. A. Khaleel, Computer simulations of interstitial loop growth kinetics in irradiated bcc Fe, Journal of Nuclear Materials 427 (2012) 259–267. doi:10.1016/j.jnucmat.2012.05.004.

[4] G. S. Was, Fundamentals of radiation materials, Springer.

[5] T. Okita, W. G. Wolfer, A critical test of the classical rate theory for void swelling, Journal of Nuclear Materials 327 (2004) 130–139. doi:10.1016/j.jnucmat.2004.01.026.

[6] A. D. Brailsford, R. Bullough, The rate theory of swelling due to void growth in irradiated metals, Journal of Nuclear Materials 44 (1972) 121–135. doi:10.1016/0022-3115(72)90091-8.

[7] P. T. Heald, M. V. Speight, Steady-state irradiation creep, Philosophical Magazine 29 (1974) 1075–1080. doi:10.1080/14786437408226592.

[8] F. A. Nichols, On the estimation of sink-absorption terms in reaction-rate-theory analysis of radiation damage, Journal of Nuclear Materials 75 (1978) 32–41. doi:10.1016/0022-3115(78)90026-0.

[9] H. Rauh, D. Simon, On the diffusion process of point defects in the stress field of edge dislocations, physica statu solidi a 42 (1978) 499–510. doi:10.1002/pssa.2210460213.

[10] L. Malerba, C. S. Becquart, C. Domain, Object kinetic Monte Carlo study of sink strengths, Journal of Nuclear Materials 360 (2007) 159–169. doi:10.1016/j.jnucmat.2006.10.002.

[11] V. Jansson, L. Malerba, A. D. Backer, C. Becquart, C. Domain, Sink strength calculations of dislocations and loops using OKMC, Journal of Nuclear Materials 442 (2013) 218–226. doi:10.1016/j.jnucmat.2013.08.052.

[12] D. Carpentier, T. Jourdan, Y. L. Bouar, M.-C. Marinica, Effect of saddle point anisotropy of point defects on their absorption by dislocations and cavities, Acta Materialia 136 (2017) 323–334. doi:10.1016/j.actamat.2017.07.013.

[13] E. Clouet, C. Varvenne, T. Jourdan, Elastic modeling of point-defects and their interaction, Computational Materials Science 147 (2018) 49–63. doi:10.1016/j.commatsci.2018.01.053.

[14] H. Rouchette, L. Thuinet, A. Legris, A. Ambard, C. Domain, Quantitative phase field model for dislocation sink strength calculations, Computational Materials Science 88 (2014) 50–60. doi:10.1016/j.commatsci.2014.02.011.

[15] H. Rouchette, L. Thuinet, A. Legris, A. Ambard, C. Domain, Influence of

shape anisotropy of self-interstitials on dislocation sink efficiencies in Zr : Multiscale modeling, Physical Review B 90 (2014) 014104. doi:10.1103/physrevb.90.014104.

[16] H. Rouchette, L. Thuinet, A. Legris, A. Ambard, C. Domain, Numerical evaluation of dislocation loop sink strengths: A phase-field approach, Nuclear Instruments and Methods in Physics Research B 352 (2015) 31–35. doi:10.1016/j.nimb.2015.01.006.

[17] L. Thuinet, H. Rouchette, A. Legris, 3D phase-field modelling of dislocation loop sink strengths, Journal of Nuclear Materials 483 (2017) 62–81. doi:10.1016/j.jnucmat.2016.10.041.

[18] P. H. Dederichs, K. Schroeder, Anisotropic diffusion in stress fields, Physical Review B 17 (1978) 2524. doi:10.1103/physrevb.17.2524.

[19] C. N. Tome, H. A. Cecatto, E. J. Savino, Point-defect diffusion in a strained crystal, Physical Review B 25 (1982) 7428–7440. doi:10.1103/physrevb.25.7428.

[20] E. J. Savino, N. Smetniansky-De Grande, Point-defect anisotropic diffusion in strained hcp metals, Physical Review B 35 (1987) 6064–6073. doi:10.1103/physrevb.35.6064.

[21] B. C. Skinner, C. H. Woo, Shape effect in the drift diffusion of point defects into straight dislocations, Phycical Review B 30 (1984) 3084–3097. doi:10.1103/physrevb.30.3084.

[22] A. Vattré, T. Jourdan, H. Ding, M.-C. Marinica, M. J. Demkowicz, Non-random walk diffusion enhances the sink strength of semicoherent interfaces, Nature Communications 7 (2016) 10424. doi:10.1038/ncomms10424.

[23] C. Jiang, N. Swaminathan, J. Deng, D. Morgan, I. Szlufarska, Effect of grain boundary stresses on sink strength, Materials Research Letters 2 (2013) 100–106. doi:10.1080/21663831.2013.871588.

[24] M. Rose, A. G. Balogh, H. Hahn, Instability of irradiation induced defects in nanostructured materials, Nuclear Instruments and Methods in Physics Research Section B 127-128 (1997) 119–122. doi:10.1016/s0168-583x(96)00863-4.

[25] Y. Chimia, A. Iwase, N. Ishikawa, M. Kobiyama, T. Inami, S. Okuda, Accumulation and recovery of defects in ion-irradiated nanocrystalline gold, Journal of Nuclear Materials 297 (2001) 355–357. doi:10.1016/s0022-3115(01)00629-8.

[26] A. Khachaturyan, Theory of structural transformations in solids, Wiley.

[27] F. R. N. Nabarro, The synthesis of elastic dislocation fields, Philosophical Magazine 42 (1951) 1224–1231. doi:10.1080/14786444108561379.

[28] W. G. Wolfer, M. Ashkin, Stress-induced diffusion of point defects to spherical sinks, Journal of applied physics 46 (1975) 547. doi:10.1063/1.321679.

[29] V. A. Borodin, A. I. Ryazanov, C. Abromeit, Void bias factors due to the anisotropy of the point defect diffusion, Journal of Nuclear Materials 207 (1993) 242–254. doi:10.1016/0022-3115(93)90266-2.

[30] W. T. Read, W. Shockley, Dislocation models of crystal grain boundaries, Physical review 78 (1950) 275–289. doi:10.1103/physrev.78.275.

[31] C.-R. Chiang, Stress concentration around a spherical cavity in a cubic medium, Journal of strain analysis 42 (2007) 155–162. doi:10.1243/03093247jsa226.

[32] J. D. Eshelby, The determination of the elastic field of an ellipsoidal inclusion, and related problems, Proceedings of the royal society A 241 (1957) 376–396. doi:10.1007/1-4020-4499-2_18.

[33] L. Thuinet, A. D. Backer, A. Legris, Phase-field modeling of precipitate evolution dynamics in elastically inhomogeneous low-symmetry systems: Application to hydride precipitation in Zr, Acta Materialia 60 (2012) 5311–5321. doi:10.1016/j.actamat.2012.05.041.

[34] L. Thuinet, A. Legris, L. Zhang, A. Ambard, Mesoscale modeling of coherent zirconium hydride precipitation under an applied stress, Journal of Nuclear Materials 438 (2013) 32–40. doi:10.1016/j.jnucmat.2013.02.034.

[35] M.-A. Louchez, L. Thuinet, R. Besson, A. Legris, Microscopic phase-field modeling of hcp|fcc interfaces, Computational Materials Science 132 (2017) 62–73. doi:10.1016/j.commatsci.2017.02.012.

[36] G. Oum, L. Thuinet, A. Legris, A 3D crystal plasticity model for coherency loss during precipitation, Modelling and Simulation in Materials Science and Engineering 26 (2018) 065008. doi:10.1088/1361-651x/aacfdb.

[37] J. W. Cahn, On spinodal decomposition, Acta metallurgica 9 (1961) 795–801. doi:10.1016/0001-6160(61)90182-1.

[38] P. T. Heald, M. V. Speight, Point defect behaviour in irradiated materials, Acta Metallurgica 23 (1975) 1389–1399. doi:10.1016/0001-6160(75)90148-0.

[39] C. Kittel, Introduction to Solid State Physics, 8th Edition, Wiley, 2004. doi:10.1063/1.3060399.

[40] M. I. Mendelev, S. Han, D. J. Srolovitz, G. J. Ackland, D. Y. sun, M. Asta, Development of new interatomic potentials appropriate for crystalline and

liquid iron, Philosophical Magazine 83 (2003) 3977–3994. doi:10.1080/14786430310001613264.

[41] L. Malerba, M. C. Marinica, N. Anento, C. Björkas, H. Nguyen, C. Domain, F. Djurabekova, P. Olsson, K. Nordlund, A. Serra, D. Terentyev, F. Willaime, C. S. Becquart, Comparison of empirical interatomic potentials for iron applied to radiation damage studies, Journal of Nuclear Materials 406 (2010) 19–38. doi:10.1016/j.jnucmat.2010.05.017.

[42] G. Kresse, J. Hafner, Ab initio molecular dynamics for liquid metals, Physical Review B 47 (1993) 558–561. doi:10.1103/PhysRevB.47.558.

[43] G. Kresse, J. Furthmuller, Efficient iterative schemes for ab initio total-energy calculations using a plane-wave basis set, Physical Review B 54 (1996) 11169–11186. doi:10.1103/PhysRevB.54.11169.

[44] R. A. Johnson, Point-defect calculations for an fcc lattice, Physical Review 145 (1966) 423–433. doi:10.1103/physrev.145.423.

[45] C. Domain, C. S. Becquart, Ab initio calculations of defects in Fe and dilute Fe-Cu alloys, Physical Review B 65 (2001) 024103. doi:10.1103/physrevb.65.024103.

[46] A. Sivak, V. Chernov, V. Romanov, P. Sivak, Kinetic monte-carlo simulation of self-point defect diffusion in dislocation elastic fields in bcc iron and vanadium, Journal of Nuclear Materials 417 (2011) 1067–1070. doi:10.1016/j.jnucmat.2010.12.176.

[47] T. Jourdan, A. Vattré, A continuous model including elastodiffusion for sink strength calculation of interfaces, Computational Materials Science 153 (2018) 473–478. doi:10.1016/j.commatsci.2018.07.023.

[48] Y. Gu, J. Han, S. Dai, Y. Zhu, Y. Xiang, D. J. Srolovitz, Point defect sink efficiency of low-angle tilt grain boundaries, Journal of the Mechanics and Physics of Solids 101 (2017) 166–179. doi:10.1016/j.jmps.2017.01.011.

[49] P. Liu, S. Zheng, K. Chen, X. Wang, B. Yan, P. Zhang, S. Q. Shi, Point defect sink strength of low-angle tilt grain boundaries: A phase field dislocation climb model, International Journal of Plasticity 119 (2019) 188 – 199. doi:10.1016/j.ijplas.2019.03.008.

[50] C. Shen, J. Li, Y. Wang, Predicting structure and energy of dislocations and grain boundaries, Acta Materialia 74 (2014) 125–131. doi:10.1016/j.actamat.2014.03.065.

[51] J. Ke, A. Boyne, Y. Wang, C. Kao, Phase field microelasticity model of dislocation climb: Methodology and applications, Acta Materialia 79 (2014) 396–410. doi:10.1016/j.actamat.2014.07.003.

[52] P.-A. Geslin, B. Appolaire, A. Finel, A phase field model for dislocation climb, Applied Physics Letters 104 (2014) 011903. doi:10.1063/1.4860999.

[53] P.-A. Geslin, B. Appolaire, A. Finel, Multiscale theory of dislocation climb, Physical Review Letters 115 (2015) 265501. doi:10.1103/physrevlett.115.265501.

[54] P.-A. Geslin, B. Appolaire, A. Finel, Investigation of coherency loss by prismatic punching with a nonlinear elastic model, Acta Materialia 71 (2014) 80–88. doi:10.1016/j.actamat.2014.03.005.

[55] J. M. Carcione, G. C. Herman, A. P. E. T. Kroode, Seismic modeling, Geophysics 67 (2002) 1304–1325. doi:10.1190/1.1500393.

[56] E. H. Saenger, N. Gold, S. A. Shapiro, Modeling the propagation of elastic waves using a modified finite-difference grid, Wave Motion 31 (2000) 77–92. doi:10.1016/s0165-2125(99)00023-2.

[57] J. B. Piochaud, M. Nastar, F. Soisson, L. Thuinet, A. Legris, Atomic-based phase-field method for the modeling of radiation induced segregation in Fe–Cr, Computational Materials Science 122 (2016) 249–262. doi:10.1016/j.commatsci.2016.05.021.

- ab initio calculations

(Point defect elastic dipole tensors at stable and saddle points)

- Atomic input data for phase-field calculations

Mesoscale phase-field modelling of microstructures generating elastic fields

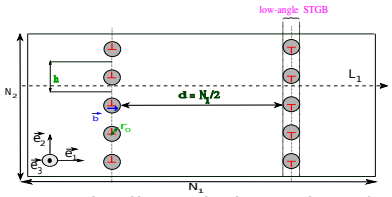

Symmetric tilt grain boundary (STGB)

Results

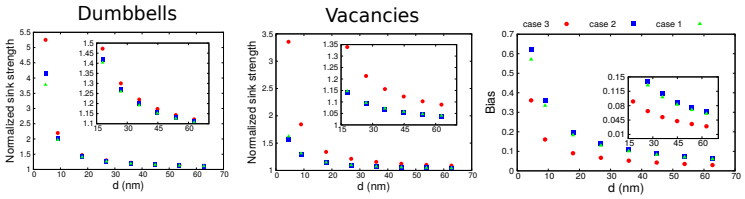

Normalized sink strengths and bias as a function of STGB interspacing in Ni. Case 1: no elastodiffusion, case2: elastodiffusion with isotropic PD at saddle point, case 3: full elastodiffusion